

# Preliminary Investigation of Power Flow and Electrode Phenomena in a Multi-Megawatt Coaxial Plasma Thruster

Kurt Schoenberg, Richard Gerwin, Ivars Henins, Robert Mayo,  
Jay Scheuer, and Glen Nurdén  
*Los Alamos National Laboratory*  
*Los Alamos, New Mexico*

March 1993

Prepared for  
Lewis Research Center  
Under Contract NAS3-30065-A



(NASA-CR-191084) PRELIMINARY  
INVESTIGATION OF POWER FLOW AND  
ELECTRODE PHENOMENA IN A  
MULTI-MEGAWATT COAXIAL PLASMA  
THRUSTER Final Report (LANL) 59 p

N93-26555

Unclass

G3/20 0159310



# Preliminary Investigation of Power Flow and Electrode Phenomena in a Multi-Megawatt Coaxial Plasma Thruster

Kurt F. Schoenberg, Richard A. Gerwin,  
Ivars Henins, Robert M. Mayo\*,  
Jay Scheuer, and Glen Wurden

Los Alamos National Laboratory  
Los Alamos, NM 87545

## Abstract

This paper summarizes preliminary experimental and theoretical research that was directed towards the study of quasi-steady-state power flow in a large, un-optimized, multi-megawatt coaxial plasma thruster. The report addresses large coaxial thruster operation and includes evaluation and interpretation of the experimental results with a view to the development of efficient, steady-state megawatt-class magnetoplasma-dynamic (MPD) thrusters.

Experimental studies utilized the Coaxial Thruster Experiment (CTX) facility at the Los Alamos National Laboratory. The un-optimized thruster, one meter in length with inner and outer tungsten-coated electrode diameters of 0.37 m and 0.56 m respectively, was operated over a range of peak power levels (nominally 10 to 40 MW) in order to ascertain high-power scaling properties. In addition to pure self-field operation, an unoptimized applied magnetic field configuration, with adjustable flux densities, was used to form a rudimentary, annular magnetic nozzle. Power distribution-relevant measurements employed a large complement of diagnostics such as spatially resolved CO<sub>2</sub> interferometry, time and space-resolved bolometry, time and space resolved electrode IR calorimetry, double-swept Langmuir probes, magnetic probes, CCD optical imaging, and time-of-flight neutral-particle spectroscopy. In this initial research, an accurate power balance was precluded due to the lack of spatial resolution of power deposition on the electrodes. However, the data, together with a calorimetric IR data reduction algorithm, did quantify energy flux deposition on electrode surfaces and provided a qualitative picture of global power flow.

---

\*Dept. of Nuclear Engineering, North Carolina State University, Raleigh NC 27695

Estimates of the active electrode surface, which proved to constitute reasonably substantial fractions of the total electrode area, indicated that the discharge was well distributed over the electrode surfaces.

In support of the experimental research, a preliminary theoretical model of electrode power deposition was developed in conjunction with measured potential profiles. A calorimetric data-reduction algorithm was developed to convert the measured transient temperature excursions in the electrodes into estimates of peak surface power-density deposition from the plasma propellant. Kinetic estimates of the surface power-density due to the deposition of charged particle energy acquired by falling through the measured anode sheath potential drop, were in semiquantitative agreement with this algorithm. Fundamental considerations of the plasma production process were used to estimate the ion temperature, and by equipartition, the electron temperature. The latter was quite comparable to the measured  $T_e$ , especially when allowing for the modest amount of microturbulent heating that may be associated with the Lower Hybrid Drift instability under the operating parameters of the device. More importantly, the measured longitudinal flow velocity of the propellant was in essential agreement with the prediction of self-field nozzle theory, achieving Alfvénic flow velocities of  $\approx 10^5$  m/s.

Other highlights of this study indicate that radiative emission is a negligible power loss mechanism ( $< 10\%$ ) over the operational power range studied. Also, preliminary measurements indicate that the magnetic topology between anode and cathode can produce a substantial influence on the electrode sheath potentials, especially on the anode fall. This thereby suggests a means for influencing the power deposited on the electrodes, with concomitant benefits to thruster efficiency, without relinquishing axisymmetry.

## I. INTRODUCTION

This report summarizes initial research performed on the Los Alamos Coaxial Thruster Experiment (CTX) facility that was directed towards establishing a perspective and understanding of quasi-steady-state power utilization in large, high-power, electro-dynamically driven plasma thrusters. Principal research objectives include developing an understanding of thruster efficiency and its dependence on device parameters such as spatial dimension, power level, mass-flow rate, and electrode sheath properties in the limit of steady-state operation. The ongoing work is motivated by the expectation that experience amassed over years of research on coaxial plasma guns could be directly applicable to the design of more efficient, steady-state, high-power magnetoplasmadynamic (MPD) thrusters.<sup>1,2</sup>

Coaxial plasma thrusters, like MPD thrusters, utilize a magnetohydrodynamic plasma acceleration mechanism to produce thrust.<sup>3,4</sup> In addition to the ionization losses and other (nominal) frozen-flow losses, thruster efficiency can be considered as limited by characteristic processes occurring in two distinct spatial regimes. One regime, which encompasses the part of the annular inter-electrode volume that is dominated by the electrode sheath potentials, is characterized by electrode power losses acquired by the localized kinetic acceleration of charged particles, and leads to undesirable power deposition on the electrodes. This regime has presented a major impediment to the development of efficient MPD thrusters.<sup>2</sup> Its study comprises a major focus of the work reported here.

The other regime involves the bulk of the annular volume containing the main flow field. As discussed below, very basic considerations regarding the main flow field show that it also can have a substantial influence on thruster efficiency, and thus its presence and nature is an important constituent of our research. This is *a fortiori* true when a global power balance is ultimately attempted. Although these two spatial regimes are mutually interactive, and may conceivably be separated by graduated spatial sub-regimes, this zero-order idealization provides an efficacious framework for the study of thruster efficiency.

## II. THE CTX FACILITY AND THRUSTER OPERATION

A photograph and schematic of the CTX coaxial plasma thruster is shown in Figure 1. Coaxial guns of this size have been extensively used as a plasma and magnetic helicity (linked magnetic flux) sources in magnetic fusion and defense program experiments at power levels exceeding 100 MW.<sup>5,6</sup> Pulsed coaxial plasma guns of similar design, albeit with different spatial and operational scales, have been flown in space to investigate the dynamic interaction of high-energy plasma with the upper atmosphere and the Earth's geomagnetic field,<sup>7</sup> as well as investigated for advanced propulsion applications<sup>8</sup> and materials processing.<sup>9</sup>

For this study, the CTX facility (Figure 1c) was configured to operate in a power range from 10 MW to 40 MW.<sup>200</sup> A 2 MJ (10kV) capacitor bank was direct-coupled through ignitron switches to the electrodes, where the outer electrode (anode) was set at the reference ground potential. A 10 to 40 MW discharge required a bank charge voltage of only 1 to 2 kV. At this low charge voltage, the banks accessed only 4% of their maximum energy capacity. Direct discharge of the banks into the thruster at this low energy, without pulse-forming networks or voltage transformers, produced "round-top" current and voltage waveforms of approximately 1 ms in duration as shown in Fig. 2. On the magnetohydrodynamic time scale for plasma evolution, however, the current and voltage were quasi-static. In this sense, the discharges were quasi-steady-state.

The CTX thruster consists of two coaxial, stainless steel, tungsten-coated electrodes. The inner and outer electrodes are 1 meter long and have diameters of 0.37 m and 0.56 m, respectively. The working gas, typically hydrogen or deuterium, is injected in the annular acceleration region by six fast puff valves that are fired roughly a millisecond before the electrodes are energized. The valves are magnetically driven in parallel by a current pulse from a small (340 J @ 2 kV) capacitor bank. They fully open in roughly 100  $\mu$ s and empty a 1 cm<sup>3</sup> volume of compressed (up to 10 atm) gas per valve. On the 1 ms discharge timescale, primary fueling is strongly influenced by gas desorption off the electrode surfaces.<sup>5</sup> The thruster is fired inside a 5 foot (dia) by 15 foot cylindrical vacuum tank. Three 500 l/s turbo-molecular pumps and three 2500l/s vacuum cryopumps maintain a base pressure of 10<sup>-6</sup> torr.

---

<sup>200</sup>Operation at power levels up to 900 MW was occasionally accessed for diagnostic calibrations and scaling insights.

Tank pressure during thruster operation remained less than one millitorr.

The center electrode (cathode) contains a solenoidal coil that produces an applied  $B_{rz}$  field (the nozzle field). The coil is driven by an ignitron switched 1.19 *mf* capacitor bank. The nozzle field rises to peak value in 6 ms at which time the discharge is initiated. The vacuum field configuration of  $B_{rz}$  is approximately constant during thruster operation. However, as discussed below, interaction of the flowing plasma with the applied field distorts the vacuum field shape and is believed to form a rudimentary magnetic nozzle.<sup>5</sup> A calculated estimate of the vacuum  $B_{rz}$  field at the time of discharge initiation is shown in Figure 3. This unoptimized  $B_{rz}$  field configuration is unconventional within MPD thruster research in that the applied magnetic field lines are intercepted by both electrodes, with a connection length estimated to be not very much larger than the interelectrode spacing ( $\Delta \approx 0.1$  m). Thus, from the MPD standpoint, the CTX plasma thruster is unusual with regard not only to size and power level, but also with regard to the applied magnetic configuration. Future research will focus on optimizing the  $B_{rz}$  field configuration with respect to optimizing thruster performance.

Diagnostics, which measure properties within the thruster and the plasma plume, included voltage and current sensors, magnetic and electrostatic probes, CCD visible imaging, x-ray imaging, infrared electrode calorimetry, multi-chord interferometry, visible spectroscopy, neutral particle spectroscopy, and wide bandwidth bolometry. This ensemble of diagnostics was chosen to address global power balance including radiative, thermal, and particle energy loss channels. Other key facility hardware were a computer-controlled safety interlock, bank-charging, and data acquisition system. Data was acquired by CAMAC based signal conditioners and digitizers.

### III. QUALITATIVE CHARACTERISTICS EXPECTED OF CTX COAXIAL THRUSTER OPERATION

Coaxial plasma thrusters have two demonstrable attributes: they produce “high-grade” (large magnetic Reynolds number), energetic plasma and they operate over a range of spatial scales. As previously discussed, both of these attributes can beneficially affect thruster performance.<sup>4</sup> Energetic plasma generation is necessary in order to meet the high specific impulse requirements of advanced space missions. Furthermore, we believe that efficient steady-state thruster operation requires “high-

grade" plasma with good coupling between the plasma and the self and applied magnetic fields. Within the context of MHD, these requirements naturally lead to an economy of scale for efficient thruster operation with respect to plasma temperature, thrust power, and spatial dimension.<sup>4</sup>

Central to efficient thruster operation is the utilization of a magnetic nozzle. For efficient acceleration of plasmas by magnetic fields, the magnetic pressure gradient must push the plasma downstream without slippage.<sup>300</sup> The primary cause of such slippage is the presence of resistance to the flow of electrical current in the plasma. This electrical resistance constitutes a dissipative property leading to a loss of efficiency. To the extent that such resistance can be made small, the plasma then approximates the ideal MHD model of a fluid endowed with high electrical conductivity. This notion can be quantified in terms of a Magnetic Reynolds Number,  $R = V\Delta/D$ , where  $V$  is the plasma axial flow velocity,  $\Delta$  is the width of the annular flow channel, and  $D = \eta/\mu_o$  is the resistive diffusivity of plasma. In the ideal MHD model,  $R$  is large compared to unity.<sup>4</sup>

The theory of nozzle flow for ideal MHD plasmas has been worked out and provides a physical picture somewhat analogous to ordinary gas-dynamic nozzle flow.<sup>10,3,4</sup> Three principal results emerge. First, the acceleration of ideal plasma can be accomplished smoothly in a graduated converging-diverging nozzle geometry. Second, the plasma reaches a characteristic velocity in the throat of the nozzle. In the absence of thermal effects and without an externally applied pervading magnetic field, this velocity is the local Alfvén speed,  $B_\theta/\sqrt{\mu_o\rho}$  (MKS), where  $B_\theta$  is the azimuthal ("self") magnetic field strength in the throat,  $\mu_o$  is the magnetic permeability of free space, and  $\rho$  is the mass density of plasma in the throat. Third, in the absence of a converging-diverging nozzle geometry, there can be no smoothly distributed macroscopic plasma acceleration within the context of the axisymmetric, steady-state, ideal MHD model. This fundamental result also proves to hold when there is a strong axial magnetic field pervading the device.<sup>10</sup>

In the absence of a nozzle, acceleration occurs in nonideal velocity jumps within thin dissipative layers, wherein the electrical currents and magnetic pressure gradients

---

<sup>300</sup> A somewhat similar comment applies to magnetically driven plasma spin-up in the thrusters which utilize strong applied magnetic fields. Here the swirl energy is eventually converted to axial flow energy in the diverging part of a downstream magnetic nozzle.



are concentrated. These layers thus separate uniform regions of differing flow velocities, and the high current concentrations in these layers can be injurious to the electrodes.<sup>301</sup> Moreover, such current sheets are known to be unstable to filamentation. In contrast, the converging-diverging geometry, in principle, need only rely upon a smoothly distributed electrical current to accelerate plasma.

From the above discussion, we see that MHD plasma accelerators with straight material or magnetic walls must necessarily rely upon localized, nonideal (dissipative) properties of plasma in order to achieve plasma acceleration. Hence, MHD accelerators with straight channels, or with *ad-hoc* nozzle designs, may be unable to access the most efficient coupling of plasma propellant to the driving magnetic fields. For example, the Princeton “benchmark thruster” experiments<sup>11,12</sup> have provided informative and detailed data regarding the local concentrations of potential gradients, current densities, and heat flux at the lip of a disk-anode that forms a rudimentary annular nozzle. In this context, Gallimore<sup>12</sup> observed that a severe reduction in the nominal anode area (leaving the anode lip exposed) had minimal impact on the current-voltage characteristics of the device. This suggests that most of the arc discharge is always concentrated at the anode lip.

A properly designed nozzle geometry can, in principle, produce a smooth, gradual acceleration of plasma without relying primarily upon the presence of nonideal effects, and therefore has access to a more efficient regime of operation. Thus, any investigation of power flow channels, with a view towards optimization, should be mindful of the interrelation between nonideal power losses (including electrode losses) and the nature of the main flow field.

Such considerations are relevant to the applied magnetic field configuration in CTX, since the axial flow of electrically conducting plasma imposes a downstream distortion upon the applied vacuum magnetic field lines. In fact, there is evidence involving the “stuffing” and “unstuffing” of the CTX thruster<sup>5</sup> that when the applied magnetic field strength is of order or smaller than the nominal strength of the self-field, the plasma propellant “blows out” the applied magnetic field. This process forms, at least locally, a diverging nozzle configuration just downstream of the muzzle.<sup>5</sup> Moreover, one may expect that a converging nozzle throat may be formed just upstream

---

<sup>301</sup>In the less-ideal plasmas, such dissipative acceleration layers would, of course, become thicker or more diffuse.

of the muzzle. Here, the self-field is “used up” in accelerating the plasma, and hence is unable to completely counterbalance the transverse magnetic pressure exerted by the applied  $B_{rz}$  field.

These qualitative inferences are supported in CTX by the experimental verification of theoretical predictions for self-field-driven flows through converging-diverging annular nozzles. Measurements of the axial propellant velocity indicate flows at the Alfvén speed.<sup>4</sup> Because the CTX electrodes are straight, we hypothesize that the “nozzle” is provided by the self-consistently distorted applied magnetic field. Direct experimental measurement of the nozzle field will be explored in future work.

To the extent that the present unoptimized CTX thruster produces a magnetic-nozzle geometry that is fairly commensurate both with the flow streamlines and the equipotential surfaces, one can expect that the electrode effects of acceleration and current flow (and concomitant power losses from the plasma) will be gradually distributed on the CTX electrodes. This contrasts with thruster configurations where the arcs are concentrated in small regions having a constant characteristic location.<sup>12</sup>

## IV. ELECTRODE PHENOMENA

### A. Infrared Electrode Calorimetry

An Inframetrics model 600 IR video camera was used to monitor and quantify surface heating on the electrodes. The camera provided absolutely calibrated measurements of electrode temperature as discussed in Appendix C. Both end-on and side-on views of the cathode and anode were enabled using a combination of salt and germanium optics to image the nominal 10 micron infrared emission off the electrode surfaces.

The Inframetrics camera was operated in either an image mode (17 millisecond frame acquisition) or fast line scan (62 microsecond sweep) mode. Both temporal and spatial measurements of the heat pulse decay were made. Full coverage of the electrode surfaces, however, was not possible due to limited optical access. Temperature excursions from a few degrees Centigrade for 10 MW low power discharges, to 120 degree increases for 800 MW high power discharges, were observed. These temperature excursions were converted to peak power deposition estimates by using the calorimetric data reduction algorithm discussed in Section IV-B and in Appendix A.

In general, shot-to-shot heating nonuniformities were of order a factor of two. This variation was attributed to non-reproducible electrode heating due to surface arcing or time-dependent, non-azimuthally-symmetric discharge behavior.

Since the plasma pulse duration and decay of electrode surface heat is short compared to the frame acquisition time, the camera, in image mode, gave a distribution of temperature increase that was convoluted with the temperature decay during the frame acquisition. Thus, in order to resolve the temporal and spatial behavior of electrode heating, the camera was operated in the line-scan mode. An example of an “end-on” infrared image is shown in Figure 4.

The infrared data can be displayed as either video images or as computer-generated plots. An example of digitized line-scan data is shown in Fig. 5a. Here, time runs from top to bottom of the frame, and the spatial axis runs left-right. This data was obtained by viewing the thruster at a 60 degree angle to the cathode face normal from a side-on port. The spatial position of the line scan for this data is shown in Fig, 5b.

In Figure 5a , temperature information during the discharge (0–0.5 ms) is masked by noise. However, heat decay after the discharge is clearly visible along the time axis. The vertical axis is temperature rise, while the spatial dimension along the chosen line-scan is from left to right. Uncertainty in the spatial decay length of the temperature is primarily due to the limited viewing access, and to some extent, due to the imperfect optical resolution of the IR camera. For the data presented herein, these uncertainties precluded absolutely calibrated estimates of total electrode power absorption. Nevertheless, the IR imaging technique did provide valuable insights into the qualitative properties of electrode power deposition as discussed in Section D. We note, that this IR electrode calorimetry technique is being refined to allow for absolute power deposition measurements in future CTX experiments.

## **B. Calorimetric Data Reduction Algorithm**

In this subsection, an algorithm is constructed for converting the observed time-dependent surface-temperature increase into an energy flux incident on the local electrode surface. This algorithm is based upon two assumptions. First, the radial flux of energy out of the plasma is assumed to have the same time-dependence as the

electrical input power to the CTX device, which is idealized here as triangular, with a linear rise time to peak power,  $t_r$ , and a linear fall time from peak power,  $t_f$ . (The rise time,  $t_r$ , shall be taken as the time to reach peak power input to the device; the fall time,  $t_f$ , shall be taken as the time required for the device power to drop from its peak value to ten percent thereof.) Second, the tungsten layer of thickness 1 mm, covering each stainless steel electrode, is taken to be a semi-infinite slab on the thermal time scales of interest. This assumption is justified because the thermal time constant for a slab of thickness  $\delta$  is roughly  $0.4(\delta^2/D_{th})$ , where  $D_{th} = (\kappa/\rho C)$  is the thermal diffusivity of tungsten.<sup>401</sup> This time constant has the value of about 5.5 ms for  $\delta = 1$  mm.

For times  $t$  small compared to 5.5 ms, we therefore assume that a semi-infinite slab of tungsten is irradiated by an energy flux  $q(t)$ , linearly rising to  $q_{max}$  for  $0 < t < t_r$ , and linearly falling to zero for  $t_r < t < (t_r + t_f)$ . The problem, then, is to calculate the surface temperature rise as a function of time,  $T(t)$ . Finally, the answer to this problem is inverted to express the energy flux  $q$  in terms of the observed surface temperature rise  $T$ .<sup>402</sup>

The heat-flow problem as formulated here can be solved by applying the method of Laplace transforms to the heat-diffusion equation. One then finds the temperature rise at the plasma-electrode surface to be

$$T(\tau) = \frac{4}{3\sqrt{\pi}} q_{max} \sqrt{\frac{t_r}{\kappa\rho C}} f(\tau, \tau_f) \quad (^\circ\text{C}) , \quad (4.1)$$

where

$$\tau = t/t_r , \quad \tau_f = t_f/t_r , \quad (4.2)$$

and the function  $f(\tau, \tau_f)$  is given by

---

<sup>401</sup>Here,  $\kappa$  is the thermal conductivity,  $\rho$  is the mass density, and  $C$  is the specific heat capacity.

<sup>402</sup>Our approach differs from the previous work of Saber<sup>11</sup> and Gallimore<sup>12</sup> in two respects. First, they measured changes in temperature from the back-side of the anode (separated from the plasma by the anode wall thickness) whereas we measure temperature excursions on the anode surface directly exposed to the plasma. Second, they characterize the energy flux time-dependence as a rectangular pulse, consonant with the shape of their flat-topped current pulse. In contrast, the “round-topped” CTX discharges, discussed in this report, are best characterized by triangular energy-flux waveforms.

$$f(\tau, \tau_f) = u(\tau)\tau^{3/2} - u(\tau-1)(\tau-1)^{3/2}(1+\tau_f^{-1}) + u(\tau-1-\tau_f)(\tau-1-\tau_f)^{3/2}\tau_f^{-1}. \quad (4.3)$$

Here,  $u(x)$  is the unit step-function which vanishes for  $x < 0$  and is unity for  $x > 0$ .

For later reference, the tungsten parameters used in Eq. (4.1) are thermal conductivity  $\kappa$ , mass density  $\rho$ , and specific heat capacity  $C$ , with the standard values

$$\kappa = 1.8 \times 10^2 (\text{joule/m s } ^\circ\text{C})$$

$$\rho = 19 \times 10^3 (\text{kg/m}^3)$$

$$C = 1.3 \times 10^2 (\text{joule/kg-}^\circ\text{C}). \quad (4.4)$$

In the present discussion, we provisionally ignore the fact that the sprayed tungsten layer probably possesses some porosity, with concomitantly reduced values of mass density and thermal conductivity. This will lead us to *over-estimate* the inferred energy flux on the electrode surfaces.

Examples of the time-dependent surface temperature rise,  $f(\tau, \tau_f)$ , are shown in Figs. 6 and 7 for  $\tau_f = 5.5$  and 3.0 respectively. A characteristic feature of this time dependence is an initially rapid decay transitioning to a slow decay. A similar experimental result from a nominal 10 MW shot is illustrated in Fig. 8, which is composed of a time-sequence of repeated spatial scans, each narrow ( $60\mu\text{s}$ ) vertical strip being a single spatial scan of the IR camera. Aside from the apparent “spikes” caused by the compressed spatial display of each scan, there is some temporal structure during the decay, with a 0.25 ms characteristic time scale. This deviation from smooth behavior is not understood, but may be associated with the late-time production of localized arcs in the gas-starved phase of thruster operation following the main pulse.

In order to utilize Eq. (4.1), to associate the maximum energy flux,  $q_{max}$ , with the maximum observed surface temperature rise,  $T_{max}$ , it is necessary to obtain the maximum value of  $f(\tau, \tau_f)$ . This is shown as the dashed curve in Fig. 9, which is also well approximated by the solid straight line,

$$f_{max}(\tau_f) \approx 1 + 0.13\tau_f . \quad (4.5)$$

Finally, as a rough check, it is also of interest to estimate the time at which the peak surface temperature ought to occur according to the present simple model. This time (scaled by the rise time  $t_r$ ) is given by

$$\tau_{peak} = \frac{(1 + \tau_f)^2}{(1 + \tau_f)^2 - \tau_f^2} . \quad (4.6 - a)$$

(By setting  $\tau = \tau_{peak}$  in  $f(\tau, \tau_f)$ , one obtains  $f_{max}(\tau_f)$ .) The function  $\tau_{peak}$  is plotted in Fig. 10. For  $\tau_f \geq 1$ , it is well approximated by

$$\tau_{peak} \approx 0.49(\tau_f - 1) + 1.33 . \quad (4.6 - b)$$

Thus, for cases in which the fall time and the rise time are about the same ( $\tau_f \approx 1$ ) the surface temperature should peak after one third of the decay phase. However, for cases in which the fall time greatly exceeds the rise time,  $\tau_f \gg 1$ , the surface temperature should peak about halfway through the decay phase. These idealized model results appear to be in reasonable qualitative agreement with the observations, subject to our earlier remarks that the raw data contain some noise and structure of uncertain origin.

### C. Estimates of Plasma Potential and Anode Fall

The time resolved plasma potential was inferred from electron temperature and floating potential measurements at three different positions in 40 MW discharges using a Langmuir probe. The floating potential during each shot was digitized and recorded at the rate of 1 MHz. The probe, originally designed for use as a double, swept Langmuir probe,<sup>13</sup> consisted of two 1 mm diameter platinum probe tips separated by 3 mm and extending 1 mm beyond a boron nitride insulating mount. The plasma potential was obtained from the floating potential using the standard relation:<sup>14</sup>

$$V_{plasma} = V_{probe} + \left( \frac{kT_e}{2} \right) \ln \left( \frac{\pi m_e}{2M_i} \right) , \quad (4.7)$$

where  $kT_e$  was nominally measured at 15 eV in deuterium.<sup>404</sup>

Fig. 11 shows measurements of plasma potential made at three probe positions: (1) inside the muzzle, several millimeters from the anode; (2) inside the muzzle, 5 cm from the anode; and (3) 40 cm downstream from the exit plane. The data exhibit high frequency oscillations as well as long timescale variations. Shot to shot variations were less than 50 volts.

Power spectra of the voltage, plasma potential within the muzzle, and interferometer signal (center chord, 40 cm downstream of the exit) are shown in Fig. 12. These power spectra were ensemble averaged over 8 shots and have a nominal 250 kHz bandwidth. The oscillations in the discharge voltage and plasma potential are broad band, with a broad peak near 100 kHz. This spectral feature is too low for fundamental plasma oscillations. However, since this frequency corresponds to the reciprocal axial magnetosonic transit time, it is probably related to macroscopic plasma flow dynamics.

With respect to the slow variation of the plasma potential, the data exhibit two distinct behaviors. The plasma potential is substantially positive relative to the anode for the first 200  $\mu$ s of the discharge, indicating a significantly reversed anode fall around the time of peak power. Following a short transition period, the potential becomes negative for times greater than 250  $\mu$ s. The probe floating potential, measured at probe positions inside the muzzle, was averaged over time for these two periods and these results were averaged over an ensemble of shots taken under the same conditions. These results, along with the anode and cathode potentials, yield the potential profile in the muzzle (Fig. 13) for two different periods of the discharge. The plasma potential several millimeters from the anode (Fig. 13) is positive relative to the anode (confining plasma electrons) during the first 200  $\mu$ s of the discharge and negative for the remainder of the discharge.

The long timescale variation in the plasma potential, measured in the muzzle (Fig 11), can be qualitatively explained by investigating the evolution of the magnetic field structure during a discharge. Calculation of the vacuum magnetic field in the thruster

---

<sup>404</sup>The collisionless, thin-sheath approximation with unmagnetized ions is adequate for analyzing CTX conditions.<sup>15</sup> A clean probe surface was ensured by arc-discharge cleaning within the vacuum vessel.

at the time of a discharge is shown in Fig. 3. At discharge initiation, field lines from the coil within the cathode provide a magnetic connection from cathode to anode. Electrons are only marginally collisional (for classical Coulomb collisions) on the spatial scale of the CTX thruster. Hence, we expect the arc voltage to accelerate current carrying electrons to moderately high energies with respect to the bulk plasma electrons; forming a high-energy tail on the electron distribution function.

405

Early in the discharge, the plasma potential several millimeters from the anode is  $\approx 225$  V positive, confining the energetic electrons. As the discharge evolves, the field lines, which connect the cathode to the anode at early times, are stretched by the plasma and eventually magnetically connect the cathode to the tank wall. During this latter phase of the discharge, the magnetic connection between cathode and anode is reduced, and results in an “electron-attracting” anode sheath.

This behavior is evident in Fig. 14, which shows both the fraction of the discharge current flowing to the tank wall and the plasma potential in the muzzle. During the early portion of the discharge ( $< 200 \mu\text{s}$ ), the plasma potential several millimeters from the anode is positive (confining electrons) and the fraction of the discharge current flowing to the tank wall is  $\approx 30\%$ . For times greater than  $250 \mu\text{s}$ , the fraction of current flowing to the tank wall is  $\approx 80\%$  and the plasma potential changes sign, becoming negative (normal MPD anode fall).

The behavior of the plasma potential as a function of applied magnetic field structure shows that the presence of such an applied field can exert a very strong influence on the anode fall voltage. In fact, the anode fall can actually be reversed by a substantial amount. This effect is reminiscent of the use of external magnetic cusp fields to control the effective anode area and anode fall in ion sources.<sup>16</sup> However, in contrast to the ion source results, the magnetic configuration in CTX affected the anode fall voltage apparently without a marked loss of axisymmetry. The implication is that there may exist an optimal axisymmetric applied magnetic field configuration that minimizes the electrode fall voltages and hence minimizes the electrode power deposition.

---

<sup>405</sup>We note that a complete treatment of this physical process must include the effects of micro-turbulent beam-plasma interactions.



#### D. Power Deposition Estimates

Inverting Eq. (4.1), we have at the time when  $T(^{\circ}\text{C})$  peaks out,

$$q_{max} = \frac{3\sqrt{\pi}}{4} \sqrt{\frac{\kappa\rho C}{t_r}} \frac{T_{max}(^{\circ}\text{C})}{f_{max}}. \quad (4.8)$$

With the standard parameters for tungsten from Eq. (4.4), this expression becomes

$$q_{max} \left[ \frac{\text{joules}}{\text{s}\cdot\text{m}^2} \right] = \frac{2.8 \times 10^6}{\sqrt{t_r(100\mu\text{s})}} \frac{T_{max}(^{\circ}\text{C})}{f_{max}(\tau_f)}$$

or also,

$$q_{max} \left[ \frac{\text{MW}}{\text{m}^2} \right] = \frac{2.8}{\sqrt{t_r(100\mu\text{s})}} \frac{T_{max}(^{\circ}\text{C})}{f_{max}(\tau_f)}. \quad (4.9)$$

Here,  $t_r(100\mu\text{s})$  is the rise time of the power input to the plasma thruster expressed in units of 100  $\mu\text{s}$ . In addition, we recall that  $f_{max}(\tau_f)$  is approximately a linear function of the ratio of the decay time to the rise time, given by Eq. (4.5) with  $\tau_f = t_f/t_r$ . In principle,  $q_{max}$  and  $T_{max}$  in Eq. (4.9) are to be interpreted as peak values in time for each position on the electrode surfaces. In practice, we utilize measurements just after the shot, at around 0.5 ms, to avoid electrical interference.

The procedure discussed above, hereafter called the first procedure, assumes that the surface temperature excursion peaks at 0.5 ms. The results from our data ensemble based on this assumption are presented in Tables I and II. In reality, this assumption probably overconstrains the data ensemble. Thus, we also utilize an alternate procedure, hereafter called the second procedure, that allows for the temperature excursion to peak at an earlier time in the discharge. The second procedure uses Eq. (4.1) with  $T$  measured at 0.5 ms and  $f(\tau, \tau_f)$  evaluated at 0.5 ms without invoking any systematic offsets or time delays. Results from the second procedure are presented in Tables IA and IIA. We believe that these two procedures will bracket the energy flux estimates, with the first and second procedures yielding under and over estimates, respectively.

As an example of the first procedure, we consider shot 20383, a 10 MW class discharge. From Fig. 15, we see that the input power rises to about 15 MW in roughly 100  $\mu\text{s}$ . Moreover, the main decay of this power is essentially complete (down to 10% of peak power) by 350  $\mu\text{s}$ . Thus  $t_r \approx 100 \mu\text{s}$ ,  $t_f \approx 250 \mu\text{s}$ , and  $\tau_f \approx 2.5$ . From

Eq. (4.5), one then would estimate that  $f_{max} \approx 1.33$ . Fig. 5b, shows a schematic drawing of the line scan of the IR camera view for this shot. The scan passes just under the cathode, allowing an axial scan of the inner-anode far wall that is estimated to cover about 30 cm of length. Beyond this point the view upstream is occluded by the outer-anode near wall. In Figure 5a, a space and time-resolved record of the temperature rise on the anode is shown. Traversing from left to right at late times (6 ms), the lip of the far anode wall is clearly identified by the temperature increment at scan position 0.25, and occlusion by the near anode wall is likewise identified by the temperature decrement at scan position 0.65. The temporal and spatial temperature record is believed to be reliable for times exceeding 0.5 ms.

From Fig. 5a, we estimate the peak (vs position) temperature rise at about  $t = 0.5$  ms to be  $\approx 7.7^\circ\text{C}$  at the lip of the anode, exhibiting a spatial decrease upstream along the anode. (Here, 0.47 on the vertical axis is calibrated to  $10^\circ\text{C}$ .) The knee of the curve of  $T(^\circ\text{C})$  vs scan position (due to occlusion by the near anode wall in association with the limited resolution of the optics) occurs at about 0.65. The temperature rise at the knee is estimated to be about  $5.4^\circ\text{C}$ . Using Eq. (4.9), we thus estimate the peak (in time) energy fluxes to be

$$q_{max} (\text{anode lip}) \approx 15 \frac{\text{MW}}{\text{m}^2}$$

$$q_{max} (\text{"knee" at scan pos. 0.65}) \approx 11 \frac{\text{MW}}{\text{m}^2} \quad (4.10)$$

The axial distance from the anode lip to the position of the temperature "knee" is estimated to be about 25 cm, from which one can linearly extrapolate to a zero energy flux at  $l_z \approx 85$  cm. Using the peak  $q_{max}$  value in Eq. (4.10), one can estimate the power deposition on the anode (Anode area =  $1.76 \text{ m}^2$ ) to be given by  $(0.5 \times 15 \times 0.85 \times 1.76) \text{ MW}$ , or

$$P_{Anode}(20383) \approx 11 \text{ MW} . \quad (l_z = 85 \text{ cm.}) \quad (4.11)$$

If a like amount of power is deposited on the cathode (for which there is no information regarding this particular shot), then the power to the electrodes exceeds, by roughly 50%, the input power of 15 MW. This overestimate in total electrode power

absorption demonstrates the need for better spatial resolution of the electrode energy flux distribution.

In Tables I and II, we summarize the IR imaging parameters for an ensemble of 10 MW class and 40 MW class discharges. For each respective class, all experimentally controlled parameters (i.e. bank charge voltages, gas valve plenum pressure and timing,  $B_{rz}$  field values and timing) were fixed. The variations in measured parameters, such as peak discharge power and  $q_{max}$ , reflect statistical variations. Ensemble averaging over the discharges yielded, for the 10 MW class ensemble, values of average peak discharge power and  $q_{max}$  of  $11 \pm 2$  MW and  $12 \pm 3$  MW/m<sup>2</sup>, respectively. For the 40 MW ensemble, averaged peak discharge power and  $q_{max}$  were  $48 \pm 5$  MW and  $23 \pm 5$  MW/m<sup>2</sup>, respectively. Clearly, for both 10 and 40 MW class shots, the entire electrode surface is not absorbing the peak energy flux. Damage patterns on the electrode surfaces suggest that roughly 25% of the total electrode area of 2.9 m<sup>2</sup> is involved in high energy flux absorption.

### E. Interpretation

The standard model for anode energy deposition is based upon the use of fluid- type energy-conservation equations for electrons and ions.

$$\begin{aligned}
 & \frac{\partial}{\partial t} (\text{flow-energy density} + \text{thermal-energy density}) \\
 & + \nabla \cdot (\text{enthalpy flux} + \text{viscous power flux} + \text{heat flux}) \\
 & = \text{rate of work per unit volume performed by the electric field.} \quad (4.14)
 \end{aligned}$$

Here, the enthalpy flux is the sum of the flow and thermal energy density fluxes, plus the rate of pressure-work per unit volume performed by an element of fluid on the surrounding fluid; and the viscous power flux comes from the rate of work done by viscous forces in the velocity-shear layer. (Collision terms that ultimately cancel upon addition of the electron and ion equations have been omitted.) Orienting the  $x$  axis (radial direction) into the anode, one assumes a steady-state, 1-D model, and integrates across the anode fall from the “plasma edge” ( $x = x_p$ ) up to the surface of

the anode ( $x = x_a$ ). Adding the resulting electron and ion equations, but neglecting electron inertial and viscous terms, one finds the power density on the anode,  $P_{Anode}$ , to be expressed as (with  $\gamma = 5/3$ )

$$P_{Anode} = \left[ n_i V_{ix} \left( \frac{1}{2} m_i V_i^2 + \frac{5}{2} (T_i + T_e) \right) + q_{ix} + q_{ex} + \text{ion viscous power flux} \right]_{x=x_p} - \frac{5}{2} J_x \frac{T_e}{e} + J_x \Phi_p + \text{work function term} + \text{plasma radiation term} , \quad (4.15)$$

where the additional effects of the anode work function and radiation from the plasma have been explicitly inserted. Here,  $n_i$  is the ion number density,  $\vec{V}_i$  is the ion fluid velocity,  $\vec{q}_{i(e)}$  is the ion (electron) heat flux vector,  $J_x (< 0)$  is the uniform radial current density,  $T_{i(e)}$  is the ion (electron) temperature at  $x = x_p$ , and  $\Phi_p$  is the plasma potential relative to the anode at the nearby plasma edge,  $x = x_p$ . Thus, when  $\Phi_p < 0$ , electrons are accelerated into the anode. Abbreviated forms of Eq. (4.15) are sometimes employed to estimate electron power deposition on the anode in MPD thrusters.<sup>11,12</sup>

We maintain that the fluid description epitomized by Eq. (4.15) is inappropriate for describing electrode power absorption in CTX. The Coulomb-collision mean free path in CTX at the nominal 40 MW level is many centimeters. Moreover, the deuterium ion gyro-radius is at least of order 1 cm and the ions are highly magnetized ( $\omega_{ci} \approx 10\nu_{ii}$ ). We conclude that for electrode or sheath phenomena, the plasma propellant is highly kinetic in nature. Therefore, it is unrealistic and unreliable to employ a fluid model to describe physical processes that are occurring over kinetic distances. Were such an attempt to be made, one would immediately encounter the problem that the generally important thermal conduction and viscous terms in Eq. (4.15) become large, ill-defined, and not usable. Moreover, their use would require some prior knowledge of the thermal and velocity gradients in the vicinity of the near-anode boundary layer.

Instead, we employ a simple and fundamentally kinetic estimate of charged particle power deposition onto the anode for 40 MW class shots. We note that during peak power, these shots actually exhibit a *reversed* anode fall, wherein the plasma is positive relative to the anode by as much as 220 V (time-averaged) within several

millimeters of the anode surface. Thus, it is expected that plasma ions primarily are responsible for the observed power deposition during the peak power phase of these shots. The bulk-plasma electrons, with temperatures measured between 10 eV and 20 eV, do not play a significant role in anode heating.

The ion power deposition onto the anode in 40-MW shots can be estimated by calculating the ion thermal flux from the edge of the plasma towards the anode, and taking into account that the ions will acquire about 200 eV in falling through the reversed anode sheath. The exact ion temperature will little affect estimates of this ion thermal flux, and moreover, will prove to be only a minor addition to the 200 eV potential fall. The axial ion kinetic energy ( $\sim 100$  eV) is ignored in constructing this estimate because the radial profile of axial velocity is not well known in this device, and therefore it is possible that a boundary layer of reduced axial velocity exists adjacent to the anode. This approach will, therefore, provide a modest underestimate of the ion power deposition.

Although the axial flow energy in the main flow field will not be directly convected to the wall in a no-slip viscous boundary layer, it does supply energy for viscous heating within that layer. This extra heat will be partly conducted and convected downstream. Accurate estimates of these various effects in the highly kinetic regime would require the solution of kinetic equations for the non-Maxwellian deformations of the ion distribution function. We note that these neglected non-Maxwellian effects are driven by ion energies that do not dominate the reversed anode fall voltage, and probably contribute to only moderate increases in the estimates of ion power deposition onto the anode.

Ion temperature has not been directly measured within the thruster. Instead, it is estimated here from fundamental considerations of the plasma- production and entrainment process (see Appendix B). The  $T_i$ , so estimated, proves to yield semi-quantitative agreement with certain measurements of transverse energy in the plume. The fundamental observation here is that when a given mass at rest is abruptly legislated into a moving system of a specified velocity, simultaneous conservation of momentum and energy forces the production of heat, such that the flow energy and the thermal energy are equalized. A simple example of this phenomenon in gas dynamics is the state of a shocked gas behind a piston-driven strong shock propagating into a gas at rest. One finds there that the post-shock thermal energy density equals

the flow energy density. Similarly, ions created from neutrals at rest or moving slowly relative to the propellant in the coaxial plasma thruster suddenly find themselves in crossed  $\vec{E}$  and  $\vec{B}$  fields, forced to move at the  $E/B$  drift velocity. Irrespective of collisionality, it can then be shown that the ion thermal energy and drift kinetic energy must be equal.<sup>4</sup> (This effect is sometimes referred to as an “ion-slip” effect.)

The “stuffing vs unstuffing” property of CTX thruster operation leads us to infer that the relevant drift velocity seen by newly created ions is  $(E_r/B_\theta)$ , since the applied magnetic field must be pushed aside by the self-field magneto-plasma, and because independent measurements yield the result that  $B_z^2 \ll B_\theta^2$ . For 40 MW shots, typical values are near  $E_r \approx 4 \times 10^3$  V/m and  $B_\theta \approx 0.08$  Tesla in mid-channel, leading to initial drift velocities (created in the upstream region) of about  $0.5 \times 10^5$  m/s. For deuterium, this value corresponds to drift energies, and hence thermal energies, of about 25 eV. (Ions created near the nozzle throat at the muzzle would have drift velocities, hence thermal velocities, near the Alfvén speed, but would be swept downstream away from the muzzle.) Equating the ion thermal velocity to the drift velocity of newly-created ions, and using a representative density measurement,  $n \approx 1.0 \times 10^{20} \text{ m}^{-3}$  for 40 MW shots, we arrive at an estimate of the ion thermal flux,  $\Gamma_{thi}$ . Using the canonical expression for  $\Gamma_{thi}$ ,<sup>850</sup>

$$\Gamma_{thi} \approx \frac{1}{4} n v_{thi} = \frac{1}{8} \times 10^{25} \frac{\text{particles}}{\text{m}^2\text{-s}} . \quad (4.16)$$

Since each ion has acquired about 200 eV in falling through a gyro-radius spanning the reversed anode sheath, we arrive at an estimate of the ion power density at the anode, namely,

$$P_{Anode} \approx \Gamma_{thi} \times 200 \text{ eV} = 40 \text{ MW/m}^2 . \quad (4.17)$$

This result is in semi-quantitative agreement with the 24 to 31 MW/m<sup>2</sup> average energy flux shown in Tables I and Ia.

In summary, an algorithm has been developed to convert the observed transient surface heating of the electrodes into estimates of incident peak surface power density,

---

<sup>850</sup>The expression  $n v_{thi} / (2\sqrt{\pi})$  would be slightly more accurate for a half-Maxwellian distribution function.

and these estimates are in semiquantitative agreement with a simple model of ion thermal flux into the anode during the peak power phase with a reversed anode fall voltage.

## V. GLOBAL DISTRIBUTIONS OF POWER

### A. Radiation

A new-style windowless XUV photodiode, absolutely calibrated at the University of Washington, was used with a scanned collimator to measure the absolute radiation losses from the end of the CTX plasma thruster. The bolometer consisted of an XUV100C silicon photodiode detector, current-to-voltage preamp, fiber-optic link, vacuum housing, and pinhole aperture and collimator. These detectors have a highly stable internal quantum efficiency and flat spectral response up to 6 keV energy photons.<sup>17</sup> The XUV photodiode sensitivity is 0.275 Amps/Watt (radiation incident). The bolometer has been cross calibrated against a relatively traditional (but more insensitive and bulky) gold foil calorimeter from Los Alamos,<sup>18</sup> which was itself calibrated using a KrF pulsed laser at 248 nanometer wavelength.<sup>19</sup> The advantage of the XUV photodiode lies in its simplicity, greater sensitivity, and speed of response. Its principle disadvantage is the uncharacterized response to possible particle fluxes.

The bolometer viewed the plasma through a 100 micron diameter pinhole aperture, which was also limited by a 12 cm long, 0.79 cm diameter threaded tube to define the field of view. By taking into account the detector solid angle, correcting for the fraction of the plasma viewed, and assuming an isotropic radiation source, we calculate that only a tiny fraction of the plasma radiation ( $2.3 \cdot 10^{-11}$ ) hit the detector. In calibration, 1  $\mu$ Amp out of the detector corresponds to 700 kW of total plasma radiation, with estimated 20% absolute error bars. Noise levels were at 100 nanoamps, or lower, and the instrumental response time (with electronics package) was better than 1  $\mu$ s, but limited to 4  $\mu$ s to avoid aliasing at the digitizer.

By scanning the collimated bolometer across an end-on view of the thruster, on a shot-to-shot basis, we observed that the radiation was largely confined spatially to the anode-cathode gap (Figure 16). If one assumes isotropic emission of the radiation, and cylindrical symmetry of the emission pattern, we then infer an absolute radiative power loss of 3-6%  $\pm$  1% of the peak I-V input power to the thruster,

when operating over the 10-40 Megawatt range. In the case of extreme high power operation ( $\approx 900$  MW), the radiation fraction was observed to increase, although only to 10% of the input power. In summary, absolute calibrated bolometry gives an upper bound on the radiation losses, which range from 3-6% for 10-40 MW input power. We therefore conclude that radiation loss is a small constituent of global power flow for the modes of operation studied.

## B. Estimates of Thruster Performance

A double-swept Langmuir probe (DSP), a CO<sub>2</sub> multichord interferometer (MCI), and a time-of-flight (TOF) neutral particle spectrometer were used to ascertain the intrinsic properties of magnetized thruster-generated plasma flow. Included were measurements of electron temperature and ion density in the muzzle and plasma plume, and direct measurements of axial (longitudinal) neutral particle flow in the plume. In this section, we focus on thruster performance during nominal 40 MW operation.<sup>4</sup>

From spatially-resolved multi-chord CO<sub>2</sub> interferometry we infer that the ejected plasma plume is of order the thruster diameter at an axial position 40 cm downstream of the muzzle. This result is roughly independent of input power and depends mainly on the ratio of the applied ( $B_{rz}$ ) to self ( $B_\theta$ ) magnetic field for a given discharge. Self-field operation generally results in a density distribution that is peaked on axis. The density distribution broadens as a function of the applied to self-field ratio until the thruster reaches a limit where plasma ejection terminates. Qualitatively, this “stuffing limit” is reached when the tension along the applied  $B_{rz}$  field effectively exceeds the pressure in the self  $B_\theta$  field and prevents the net ejection of plasma. This effect is demonstrable over the entire power range of thruster operation.<sup>4</sup>

During nominal 40 MW operation, probe measurements in the plume 40 cm downstream of the muzzle at the interferometer plane suggest a mean ion density of  $\approx 3 \pm 1 \cdot 10^{19} \text{ m}^{-3}$ . Reasonable agreement exists between the DSP and MCI density estimates when the plume profile is of order the thruster diameter. DSP inferred electron temperature in the plume is between 10 eV and 15 eV.

The DSP was utilized to compare plasma parameters in the plume and muzzle at a fixed radial position of  $r \approx 0.25 \text{ m}$  (referenced to the thruster axis of symmetry). This



radial position placed the probe roughly half-way between the anode and cathode when inside the muzzle. Both temperature and density measurements in the muzzle were complicated by plasma noise and probe arcing. Nevertheless, a limited set of data provided estimates (within a factor of 2) of these parameters. The mean density at the muzzle was 3 to 4 times the downstream density. Again, for nominal 40 MW operation, the density at the muzzle was estimated at  $\approx 1.0 \pm 0.5 \cdot 10^{20} \text{ m}^{-3}$ . The electron temperature in the muzzle was  $\approx 10$  to 20 eV, similar to the value downstream.

Measurements of plasma density in the muzzle, and concomitant projections of density in the breech (from a Bernoulli flow model) allow preliminary comparisons to be made with the predicted MHD performance.

**Plasma Flow** From our previously discussed model of plasma flow in a converging-diverging magnetic nozzle, the plasma flow should be Alfvén like ( $V_e \approx \sqrt{2}C_{Ab}$ ).<sup>4</sup> Measurements of the axial neutral flow were made with the time-of-flight spectrometer. An example of a TOF arrival time distribution is shown in Fig. 17. The difference between the first signal spike at 135  $\mu\text{s}$  (the timing fiducial) and the second large signal spike at 153  $\mu\text{s}$  (arrival of the neutral particle flux) corresponds to an axial flow velocity of  $\approx 1.0 \pm 0.3 \cdot 10^5 \text{ m/s}$ . Furthermore, the narrow shape of the spike is indicative of an energy distribution where the directed flow energy is larger than the longitudinal thermal energy.<sup>4</sup>

In comparison, the estimated Alfvén velocity, based on density measurements in the muzzle, was  $C_{A0} \approx 0.9 \pm 0.2 \cdot 10^5 \text{ m/s}$ . The MHD model predicts a flow velocity for fully accelerated ions of  $V_e = \sqrt{3}C_{A0} \approx 1.5 \pm 0.4 \cdot 10^5 \text{ m/s}$ ,<sup>4</sup> and is in reasonably good agreement with the neutral particle velocity data. In contrast, the  $\mathbf{E} \times \mathbf{B}$  drift velocity for this discharge has an upper limit in the breech of  $V_{EB} \leq E_r/B_\theta \approx 0.5 \cdot 10^5 \text{ m/s}$ . In general, the axial neutral flow velocity is observed to exceed the  $\mathbf{E} \times \mathbf{B}$  drift velocity in the breech by a factor of 2 to 3 early in the discharge when the thruster is far from the stuffing limit. The basic agreement between the measured flow velocity and the MHD model prediction suggests that converging-diverging nozzle flow may be an important constituent of gross plasma acceleration in the present CTX thruster.

**Plasma Quality and Electrical Effort** The measured values of plasma density,

temperature, and flow velocity allow an assessment of “plasma quality”. Assuming classical resistivity, these values project a magnetic Reynolds number of approximately 1300, indicating good coupling between the plasma propellant and the magnetic fields.

Another important operational parameter is the number of elementary electrical charges that must be transferred between the coaxial electrodes for each ion-electron pair of propellant that is ejected downstream (for thrust). This quantity, which we term the Electrical Effort  $\Xi$ , may be expressed as a dimensionless number,

$$\Xi = (m_i/e)(I/\dot{M}) . \quad (5.1)$$

where  $m_i$  is the mass of a propellant ion,  $e$  is the elementary electron charge,  $\dot{M}$  is the mass flow, and  $I$  is the discharge current. A large value for the electrical effort means that large discharge currents are required to process a given mass throughput, with concomitant wear and tear on the electrodes. Thus, the reciprocal of the electrical effort can be thought of as a figure of merit for any electrodynamic thruster.

If the measured neutral particle flow velocity accurately indicates the plasma flow velocity at the muzzle, the estimated mass flow, based on the density and flow velocity measurements, is  $\dot{M} = 2\pi\rho_m V_m r_m \Delta \approx 4.5 \text{ gm/s}$ . Here,  $\rho_m$  and  $V_m$  are the mean plasma density and flow velocity in the muzzle, respectively,  $r_m$  is the mid-channel radius, and  $\Delta$  is the channel width. This gives an electrical effort of  $\Xi \approx 0.5$ . These values of  $R_M$  and  $\Xi$  are indicative of fairly high-grade plasma and consistent with the observed ideal MHD-like thruster performance.

**Thrust Power and Efficiency** With all due regard to relevant uncertainties in the experimental measurements and technique, it is interesting to note that the combination of the measured axial flow velocity and the estimated mass flow rate yields a peak thrust power estimate of 23 MW. The corresponding peak thrust for these conditions is 500 Nt. This value is close to that calculated from the MHD model which predicts an upper thrust limit of 580 Nt.<sup>4</sup>

Thruster efficiency,  $\epsilon$ , can be defined in terms of the electrical effort,  $\Xi$ , as

$$\epsilon = \frac{\varepsilon_z}{\Xi V_d} . \quad (5.2)$$

where  $\varepsilon_z$  is the mean axial energy of the propellant (in volts) and  $V_d$  is the electrical discharge voltage that appears across the electrodes of the thruster. From this expression, we conclude that the electrical effort must always exceed the ratio of the ejected energy per particle (in volts) to the discharge voltage. For the 40 MW class discharges, our 0.5 estimate for  $\Xi$ , coupled with a measured axial flow energy of  $\approx 100$  eV (for deuterium) and nominal discharge voltages of  $\approx 400$  V, projects a thrust production efficiency of  $\approx 50$  %. This value lies within the range of efficiencies reported for pulsed, high power coaxial plasma thruster operation in xenon.<sup>8</sup>

### C. Thermal Plume Losses

**Plasma Heating** As previously discussed, ion entrainment in a flow field coupled with ion- electron equipartition results in plasma heating. The observed 10 eV to 20 eV electron temperature in the muzzle is understandable from this perspective. Over the 10 MW to 40 MW discharge conditions, ion temperature is predicted to reside in a 25 eV to 45 eV range as compared to axial flow energies of 100 eV to 200 eV (see Appendix B). However, for energies exceeding 20 eV, the electrons effectively decouple from the ions as their classical equipartition time exceeds their axial transit time. Hence, the observations of electron temperature in the 10 eV to 20 eV range are consistent with heating to their equipartition limit by the higher temperature ions. They are also consistent with the estimated ineffectiveness of classical ohmic heating on the timescale of an electron axial transit.<sup>4</sup> It is possible that a moderate contribution to the electron temperature is provided by microturbulence associated with the Lower Hybrid Drift and related instabilities; and by heating due to collective interactions with primary electrons from the cathode. These issues will be discussed in future work.

## VI. SUMMARY

In summary, various measurements and associated theoretical interpretations have been implemented in a preliminary investigation of power-flow in the CTX plasma thruster. The results are, so far, constrained by the limited number of measurements taken, the uncertainty inherent in certain measurements (e.g., the active electrode area), the lack of instantaneous mass flow control, the unoptimized electrical circuitry driving the thruster, and the unoptimized nature of the applied magnetic field config-

uration. These constraints will be addressed in future research by ongoing upgrades in the electrical circuitry and mass flow control that will drive flat-topped, long-pulse ( $\approx 10$  ms) discharges at 1 to 40 MW.

In our preliminary investigation, good agreement was found between the measured properties of CTX thruster operation and the predictions of a model based on ideal MHD. This agreement suggests that ideal MHD processes play an important role in coaxial plasma thruster dynamics. Within this context, CTX performance with respect to propellant flow velocity, thrust production, and operational impedance are reasonably well understood. Interpretation of the preliminary data also reinforces our belief that optimized magnetic nozzle design can be beneficial to thruster efficiency. Related considerations carried on in parallel to this work have lead to the conceptual design of an electrically adjustable, axisymmetric, annular magnetic nozzle that is intended to address the simultaneous control of plasma acceleration, electrode sheath potentials, and plasma detachment.

It is likely that the perceptions and concepts presented in this paper have efficacy in the development of efficient, megawatt-class MPD thrusters. Specifically, designing MPD thrusters (in power and spatial scale) to access efficient plasma-magnetic field coupling and utilizing an optimized  $B_{rz}$  field configuration to maximize efficiency and minimize anode fall could prove advantageous. (We note that these perceptions are consonant with previous quasi-one-dimensional analysis of flow channel geometry effects on MPD thruster performance.<sup>20</sup>) Future coaxial thruster research will focus on these issues in the context of scaling multi-megawatt thruster performance to the smaller spatial scales and operational power levels required for MPD devices.

## VII. ACKNOWLEDGEMENTS

The authors appreciate the insights provided by Drs. David Fradkin and Robin Gribble of the Los Alamos National Laboratory, and Dr. Roger Myers of the NASA Lewis Research Center. This work was supported, in part, by the NASA Lewis Research Center Low Thrust Propulsion Group and references work supported by the U.S. Department of Energy.

## VIII. REFERENCES

- <sup>1</sup>J. S. Sovey and M. A. Manteniaks. "Performance and Lifetime Assessment of Magnetoplasmadynamic Arc Thruster Technology." *J. Propulsion*, 7(1):71, 1991.
- <sup>2</sup>R. M. Myers. "Applied Field MPD Thruster Geometry Effects." *27<sup>th</sup> Joint Propulsion Conference*, Sacramento, CA, Technical Report **AIAA 91-2342**, 1991.
- <sup>3</sup>R. A. Gerwin, G. J. Marklin, A. G. Sgro, and A. H. Glasser. *Characterization of Plasma Flow Through Magnetic Nozzles*. Technical Report **AL-TR-89-092**, Air Force Astronautics Laboratory, 1990.
- <sup>4</sup>K. F. Schoenberg, R. A. Gerwin, Cris Barnes, Ivars Henins, Robert M. Mayo, Ronald W. Moses Jr., Richard Scarberry, and Glen A. Wurden. *Coaxial Plasma Thrusters for High Specific Impulse Propulsion*. Technical Report **AIAA 91-3770**, American Institute of Aeronautics and Astronautics, 1991, submitted for publication in the AIAA Journal of Power and Propulsion.
- <sup>5</sup>C. W. Barnes, T. R. Jarboe, G. J. Marklin, S. O. Knox, and I. Henins. "Impedance and Energy Efficiency of a Coaxial Magnetized Plasma Source for Spheromak Formation and Sustainment." *Phys. Fluids B*, 2(8):1871, 1990.
- <sup>6</sup>J. C. Fernandez. *Review of Advances in Spheromak Understanding and Research*. Technical Report **LA-UR-90-1820**, Los Alamos National Laboratory, 1990.
- <sup>7</sup>R. S. Caird, C. M. Fowler, W. B. Garn, I. Henins, J. C. Ingraham, R. A. Jeffries, D. M. Kerr, J. Marshall, and D. B. Thomson. *Payload Development for a High Altitude Plasma Injection Experiment*. Technical Report **LA-4302-MS**, Los Alamos National Laboratory, 1969.
- <sup>8</sup>B. Gorowitz, T. W. Karras, and P. Gloersen. "Performance of an Electrically Triggered Repetitively Pulsed Coaxial Plasma Engine." *AIAA Journal*, 4(6):1027, 1966.
- <sup>9</sup>Y. V. Skvortsov. "Research on Pulsed and Steady-State Plasma Guns and Their Applications in the Troitsk Branch of Kurchatov Institute of Atomic Energy." *Phys. Fluids B*, 4(3):750, 1992.

- <sup>10</sup>A. I. Morozov and L. S. Solov'ev. "Steady-State Plasma Flow in a Magnetic Field." in *Reviews of Plasma Physics*, Vol. 8, edited by M.A. Leontovich, (Consultants Bureau, NY, 1980).
- <sup>11</sup>A.J. Saber and R. G. Jahn; *Anode Power Deposition in Quasi-Steady MPD Arcs*, 10th AIAA Electric Propulsion Conference, Lake Tahoe, Nevada, Technical report **AIAA-73-1091**, (1973).
- <sup>12</sup>A. D. Gallimore, A. J. Kelly, and R. G. Jahn; *Anode Power Deposition in MPD Thrusters*, 22nd International Electric Propulsion Conference, Viareggio, Italy, Technical report **IEPC 91-125**, (1991).
- <sup>13</sup>J. C. Ingraham, R. F. Ellis, J. N. Downing, C. P. Munson, P. G. Weber, and G. A. Wurden. "Energetic Electron Measurements in the Edge of a Reversed-Field Pinch." *Phys. Fluids B*, **2**(1):143-159, 1990.
- <sup>14</sup>F. F. Chen, in *Plasma Diagnostic Techniques*, edited by R. H. Huddleston and S. L. Leonard (Academic, New York, 1965), pp. 191-194.
- <sup>15</sup>P. M. Chung and L. Talbot and K. J. Touryan, *Electric Probes in Stationary and Flowing Plasmas*, (Springer-Verlag, 1975).
- <sup>16</sup>K. W. Ehlers and K. N. Leung. "Characteristics of the Berkeley Multicusp Ion Source." *Rev. Sci. Inst.*, **50**(11):1353, 1979.
- <sup>17</sup>R. Korde and L. R. Canfield. "Silicon Photodiodes With Stable, Near-Theoretical Quantum Efficiency in the Soft X-Ray Region." *SPIE*, **1140**:126, 1989.
- <sup>18</sup>J. C. Ingraham and G. Miller. "Infrared Calorimeter for Time-Resolved Plasma Energy Flux Measurement." *Rev. Sci. Instrum.*, **54**(6):673-676, 1983.
- <sup>19</sup>R. J. Maqueda and G. A. Wurden. "Wideband Silicon Bolometers on the LSX Field Reversed Configuration (FRC) Experiment." in proceedings of the Santa Fe High Temperature Plasma Diagnostics Conference, March 23-27, 1992, to be published in the Reviews of Scientific Instruments.
- <sup>20</sup>M. Martinez-Sanchez. "Structure of Self-Field Accelerated Plasma Flows." *J. Propulsion*, **7**(1):56, 1991.

## Appendix A

### Derivation of the Algorithm for Converting Surface Temperature into Incident Energy Flux.

The energy conservation equation that governs heat diffusion in a material free of internal heat sources (and sinks) is

$$\rho C \frac{\partial T}{\partial t} = -\nabla \cdot \vec{q} , \quad (\text{A-1})$$

where  $T$  is the local temperature,  $\rho$  is the local mass density,  $C$  is the heat capacity per unit mass (specific heat capacity), and  $\vec{q}$  is the local internal heat flux.

This local heat flux,  $\vec{q}$ , is related to the local temperature gradient,  $\nabla T$ , by

$$\vec{q} = -\kappa \nabla T , \quad (\text{A-2})$$

where  $\kappa$  is the local thermal conductivity of the material.

Combining (A-1) and (A-2) assuming uniform  $\kappa$ , one obtains the equation for temperature diffusion in a one-dimensional slab model, namely,

$$\frac{\partial T}{\partial t} = D_{\text{th}} \frac{\partial^2 T}{\partial x^2} , \quad (\text{A-3})$$

wherein the thermal diffusivity of the material,  $D_{\text{th}}$ , is defined by

$$D_{\text{th}} \equiv \frac{\kappa}{\rho C} . \quad (\text{A-4})$$

We shall henceforth assume that  $\rho$  (as well as  $\kappa$ ) is uniform, so that  $D_{\text{th}}$  is uniform. Concomitantly, we shall assume that  $\kappa$ ,  $\rho$ , and  $C$  are all independent of the (nonuniform) temperature, which is a good approximation over the limited range of temperature excursions that were observed on the CTX electrodes (10° C–20° C, for the 10–40MW operating range). Moreover, we note that the symbol,  $T$ , in Eq. (A-3), obviously can be interpreted as the temperature *excursion* away from the initial, uniform temperature; or more generally, as the temperature difference from any convenient reference temperature.

We shall now characterize the thickness of the tungsten electrode coating ( $\approx 1$  mm) within the context of a heat diffusion problem for which the surface irradiation time is very short. The *intrinsic thermal time constant* for a slab of

thickness  $\delta$  having thermal diffusivity  $D_{th}$ , is of order  $\delta^2/D_{th}$ , since  $\delta$  and  $D_{th}$  are the only characteristic quantities in the diffusion problem when the external conditions are changed very rapidly compared to  $\delta^2/D_{th}$ . Additional detailed considerations sketched here show that the effective thermal time constant is more accurately represented by about  $0.4\delta^2/D_{th}$ . For example, consider the situation in which a slab is initially at some given uniform temperature, but for which the temperature of one side (the “near” side) is suddenly lowered (by external forcing) to a new value and then held there. (If the near-side temperature were to be suddenly raised instead of lowered, the problem could be trivially reformulated so as to be identical to the present case.) Assuming that the far side of the slab is insulated, how long will it take for the temperature of the far side to approach the new temperature of the “near” side? This problem may be solved by expanding the function of position,  $x$ , and time,  $t$ , namely  $T(x,t)$ , in a spatial cosine series with time-dependent coefficients, each term of which satisfies both boundary conditions. Using Eq. (A-3), one finds that the slowest-decaying mode is the cosine term having only one-quarter wavelength in the slab, for which the decay time is  $(4/\pi^2)(\delta^2/D_{th})$ . This global mode makes the major contribution to the decay of the temperature at the far side. (The higher modes, which are of significantly smaller magnitude, are more relevant to the decay of “sharpness” of the square corner of the temperature profile at the near side.) This elementary viewpoint of the thermal time constant of a slab is borne out by numerical solutions.

For example, consider the problem more relevant to our situation, a slab initially at some uniform temperature, suddenly irradiated at time  $t = 0$  by a constant heat flux at the near side ( $q(t) = 0$  for  $t < 0$ ,  $q(t) = q_0$  for  $t > 0$ ). Detailed numerical solutions of the time-dependent temperature profile for this particular problem, in which the far side is insulated, can be found in the book *Unified Analysis and Solutions of Heat and Mass Diffusion* by M. D. Mikhailov and M. N. Özişik, John Wiley and Sons, 1984, Fig. 7.4-a, page 302. There, normalized time  $\tau$  is expressed in units of  $(\delta^2/D_{th})$ . One sees clearly from this figure that, for times  $\tau \lesssim 0.4$ , the temperature of the far side remains very small compared to the temperature of the irradiated side; whereas for increasing  $\tau$ ,  $\tau > 0.4$ , the continuously increasing temperatures of the two sides become comparable. (Detailed numerical solutions to the preceding problem of a sud-



denly lowered surface temperature are presented in Fig. 7.1-a on page 289 of the above reference. One again finds that  $\tau = 0.4$  constitutes a reasonable characteristic time beyond which the “far” side is influenced by the new temperature of the “near” side.) Thus  $0.4\delta^2/D_{\text{th}}$  constitutes a reasonable time-demarcation for the effective thermal time constant for heat diffusion in a slab.

The conclusion that can be drawn from the above discussion is that, for surface irradiation times (and observation times) short compared with  $0.4\delta^2/D_{\text{th}}$ , one can effectively regard the slab as being very thick (semi-infinite). Since the thermal time constant for a 1-mm-thick tungsten layer is about 5 ms, and since the CTX pulse duration is  $\lesssim 1$  ms, and since our observation times will be focused around 0.5–1 ms from “turn-on” time, we shall justifiably invoke the simplification that the tungsten layer is indeed semi-infinite within the context of highly transient heat diffusion induced by a short pulse of one-sided irradiation.

Using the above simplification, we shall now derive the solution for the time-dependent surface temperature rise induced by a time-dependent energy flux incident on the surface. The method used is the application of the Laplace transform to the temperature diffusion equation, with the use of appropriate boundary conditions.

Define a normalized time  $\tau$  by  $\tau = D_{\text{th}}t$  (with the dimension of length-squared). Then Eq. (A-3) becomes

$$\frac{\partial T}{\partial \tau} = \frac{\partial^2 T}{\partial x^2} . \quad (\text{A-5})$$

This diffusion equation is to be solved for the surface temperature excursion (at  $x = 0$ ), subject to the initial condition that

$$T(x, 0) = 0 , \quad (\text{A-6})$$

(in which  $T = 0$  constitutes the ambient reference temperature level); and the boundary condition at the “near” side,

$$\left( \frac{\partial T}{\partial x} \right)_{x=0} = -\frac{1}{\kappa} q(\tau) , \quad (\text{A-7})$$

wherein the time-dependent energy flux,  $q(\tau)$ , incident on the near surface at  $x = 0$ , will be specified later below. The boundary condition at the very distant boundary (the “far” side) will be taken as

$$T(\infty, \tau) = 0 , \quad (\text{A-8})$$

in accordance with the transient approximation discussed above.

Recalling that the Laplace transform is defined by

$$\theta(x, p) \equiv \mathcal{L}_p [T(x, \tau)] \equiv \int_0^\infty T(x, \tau') e^{-p\tau'} d\tau' ,$$

wherein  $\text{Re}(p) > 0$ , one takes the transform of Eq. (A-5) (noting the initial condition Eq. (A-6)) and finds

$$\frac{d^2 \theta}{dx^2} = p\theta , \quad (\text{A-9})$$

with the general solution

$$\theta(x, p) = A_p e^{x\sqrt{p}} + B_p e^{-x\sqrt{p}} . \quad (\text{A-10})$$

Without loss of generality, we shall use the convention that when  $\text{Re}(p) > 0$ ,  $\text{Re}(\sqrt{p}) > 0$ . At far distant positions, the temperature excursion  $T(x, \tau)$  would vanish, and so its transform should vanish out there as well (i.e., both  $T$  and  $\theta$  should vanish as  $x \rightarrow \infty$ ). Therefore, the coefficient  $A_p$  must vanish identically. Thus,

$$\theta(x, p) = B_p e^{-x\sqrt{p}} . \quad (\text{A-11})$$

Taking the transform of Eq. (A-7), one finds

$$\left( \frac{d\theta}{dx} \right)_{x=0} = -Q(p) , \quad (\text{A-12})$$

wherein

$$Q(p) \equiv \mathcal{L}_p \left[ \frac{q(\tau)}{\kappa} \right] . \quad (\text{A-13})$$

Use of (A-11) in (A-12) yields the  $B_p$ -coefficient as

$$B_p = \frac{Q(p)}{\sqrt{p}} . \quad (\text{A-14})$$

Therefore, from Eq. (A-11), the transform of the *surface* temperature (at  $x = 0$ ) is

$$\theta(0, p) = \frac{Q(p)}{\sqrt{p}} . \quad (\text{A-15})$$

In a well-defined problem, this expression should comprise a well-defined analytic function for  $\text{Re}(p) > 0$ . The time-dependent *surface* temperature itself is then obtained from the inverse Laplace transform as

$$T(0, \tau) = \frac{1}{2\pi i} \int_C \frac{Q(p)}{\sqrt{p}} e^{p\tau} dp , \quad (\text{A-16})$$

wherein the integration contour,  $C$ , is comprised of a line parallel to the imaginary axis in the complex  $p$ -plane, along which  $\text{Re}(p) > 0$ . The contour  $C$  is taken to lie to the right of all singularities of  $(Q(p)/\sqrt{p})$ , and we note that the presence of  $\sqrt{p}$  places a branch cut along the negative- $p$  axis. (Recall that  $Q(p)$  is essentially the transform of the incident energy flux.)

It also is very important to note that the integrand in (A-16) is usually a well-defined analytic function of  $p$  when  $\text{Re}(p) > 0$ , because the Laplace transform integrals are themselves well-defined and convergent when  $\text{Re}(p) > 0$  with  $\text{Re}(p)$  sufficiently large. Consequently, for  $\tau < 0$ , one may close the  $C$  contour at infinity in the right half-plane ( $\text{Re}(p) > 0$ ) so that  $|\exp(p\tau)| \rightarrow 0$  at large  $|p|$  to find that, since there are no enclosed singularities,

$$T(0, \tau) = 0 \text{ for } \tau < 0 . \quad (\text{A-17})$$

The integrand, considered as a function of the complex variable,  $p$ , is to be “analytically continued” into the left half-plane. Now, after the initial time, for  $\tau > 0$ , one can only close the contour at infinity in the left half-plane (wherein  $|\exp(p\tau)| \rightarrow 0$  at large  $|p|$ ), thereby enclosing the singularities of the integrand. Thus for  $\tau > 0$ , one generally finds that  $T(0, \tau) \neq 0$ .

To obtain a definite result, one needs to know  $Q(p)$ , and it is therefore convenient to utilize a specific and simple model for the time-dependence of the energy flux on the surface. One might, at first, think that this must be done because the “backwards” unfolding problem of inferring a time-dependent incident energy flux from a known time-dependent surface temperature response might not have a unique answer. That is, because the instantaneous surface temperature depends upon the entire past history of the incident energy flux

in the form (obtained from (A-16) and (A-13) by means of certain Laplace transform relations),

$$T(0, \tau) = \frac{1}{\kappa\sqrt{\pi}} \int_0^\tau \frac{q(\tau') d\tau'}{\sqrt{\tau - \tau'}} , \quad (\text{A-18})$$

it might be that several distinct irradiation histories could produce the same temperature response. (In more detail, we replace  $Q(p)$  in (A-16) by the explicit transform, (A-13), interchange the order of integrations and note that  $p^{-1/2}$  and  $(\pi\tau)^{-1/2}$  constitute a transform pair.) This past-history integral represents the surface temperature response of a half-space irradiated at the surface by a time-dependent heat flux,  $q(\tau')$ . However, the inversion of Eq. (A-18) proves to be well-defined and unique! One finds (see, for example, *The Mathematics of Physics and Chemistry*, by H. Margenau and G. M. Murphy, D. Van Nostrand Co. (1956); Chap. 14),

$$q(\tau) = \frac{\kappa}{\sqrt{\pi}} \frac{d}{d\tau} \int_0^\tau \frac{T(0, \tau') d\tau'}{\sqrt{\tau - \tau'}} , \quad (\text{A-19})$$

wherein we recall that  $\tau \equiv D_{\text{th}} t$ . Thus, one could, in principle, infer the time-dependent energy flux incident on the surface from sufficiently accurate surface temperature data.

The existence of a unique inversion to Eq. (A-18) is a nontrivial result, for it implies that there exists *no* time-dependent function (except “zero”), say  $\Delta q(\tau')$ , for which

$$\int_0^\tau \frac{\Delta q(\tau') d\tau'}{\sqrt{\tau - \tau'}} = 0$$

for all positive values of  $\tau$ .

In the present experimental situation, though, the temperature data probably are not known well enough to be practically utilized in a singular integration followed by a differentiation, as in Eq. (A-19). Therefore, we shall revert to solving the “forward” problem by assuming a reasonable, parameterized model for the time-dependence of the incident energy flux, and thereby shall calculate the surface temperature response. The parameters of the incident energy flux then are to be adjusted so that the computed temperature response agrees with the observations.

Our algorithm will be based upon two assumptions. First, the time dependence of the incident energy flux will be assumed as triangular, with a linear rise time  $t_r$  to a peak flux,  $q_{\max}$ , immediately followed by a linear decay over a time duration  $t_f$ . Second, the "rise" time,  $t_r$ , and the "fall" time,  $t_f$ , are to be taken from the time dependence of the power pulse into the CTX plasma gun, which itself proves to be roughly triangular. Thus, the only adjustable parameter in this simple but convenient model is  $q_{\max}$ . Accordingly,

$$q(\tau) = q_{\max} \frac{\tau}{\tau_r} \quad \text{for } (0 < \tau < \tau_r) \quad (\text{A-20-a})$$

$$q(\tau) = q_{\max} \left(1 - \frac{\tau - \tau_r}{\tau_f}\right) \quad \text{for } (0 < \tau - \tau_r < \tau_f) \quad (\text{A-20-b})$$

$$q(\tau) = 0 \quad \text{for } (\tau_f < \tau - \tau_r) . \quad (\text{A-20-c})$$

The Laplace transform of  $q(t)/\kappa$  as defined by Eq. (20), may be calculated by utilizing simple integrations and elementary algebra. The result is

$$Q(p) \equiv \int_0^\infty \frac{q(\tau)}{\kappa} e^{-p\tau} d\tau = \frac{q_{\max}}{\kappa} \left\{ \frac{1}{p^2 \tau_r} - \frac{e^{-p\tau_r}}{p^2} \left[ \frac{1}{\tau_r} + \frac{1}{\tau_f} \right] + \frac{e^{-p(\tau_r + \tau_f)}}{p^2 \tau_f} \right\} . \quad (\text{A-21})$$

This  $Q(p)$  is a well-defined analytic function for  $\text{Re}(p) > 0$ , as is also  $Q(p)/\sqrt{p}$ . The singularity of  $Q(p)/\sqrt{p}$  is at the origin of the complex  $p$ -plane, and there is a branch cut along the negative- $p$  axis. The inverse transform that yields the time-dependent temperature excursion on the tungsten surface is accordingly given by Eq. (A-16). Now, Eq. (A-21) contains three terms. Each of the three resulting contour integrals from (A-16) evidently has the form

$$\text{Integral Term}(j) = \frac{1}{2\pi i} \int_C \frac{e^{p\tau_j}}{p^{5/2}} dp, \quad j = 1, 2, 3, \quad (\text{A-22})$$

in which the contour of integration,  $C$ , is parallel to the  $\text{Im}(p)$  axis and lies just to the right of the origin ( $\text{Re}(p) > 0$  and  $\text{Re}(p) \rightarrow 0$ ). Here, the  $\tau_j$ 's are obviously defined by (see Eq. (A-16))

$$\tau_1 \equiv \tau; \quad \tau_2 \equiv \tau - \tau_r; \quad \tau_3 \equiv \tau - \tau_r - \tau_f. \quad (\text{A-23})$$

Now, in all three cases, these integrals respectively vanish identically *unless* their respective  $\tau_j$ 's are positive,  $\tau_j > 0$ , in view of the discussion just preceding Eq. (A-17). For times such that  $\tau_j > 0$ , the contour  $C$  may be deformed to lie

just below the negative- $p$  axis, to pass around the origin in a counter-clockwise manner, and thence to pass again to infinity lying just above the negative- $p$  axis. Making the change of variable of integration from  $p$  to  $p' \equiv p\tau_j$ , Eq. (A-22) becomes

$$\text{Integral Term}(j) = \tau_j^{3/2} \frac{1}{2\pi i} \int_C \frac{e^{p'}}{(p')^{5/2}} dp' . \quad (\text{A-24})$$

Finally, changing the variable of integration from  $p'$  to  $p'' = (-p')$ , and correspondingly changing to the appropriate integration contour in the  $p''$ -plane, the factor multiplying  $\tau_j^{3/2}$  may be trivially identified to be  $1/\Gamma(5/2)$ . (See, for example, *Modern Analysis*, by E. T. Whittaker and G. N. Watson, Cambridge University Press (1952); Chap. 12, esp. p. 245.) Therefore, the use of (A-21) in (A-16) provides the following expression for the surface temperature excursion.

$$T(0, \tau) = \frac{q_{\max}}{\kappa\Gamma(\frac{5}{2})} \left\{ \frac{u(\tau)}{\tau_r} \tau^{3/2} - \frac{u(\tau - \tau_r)}{\tau_r} \left( 1 + \frac{\tau_r}{\tau_f} \right) (\tau - \tau_r)^{3/2} + \frac{u(\tau - \tau_r - \tau_f)}{\tau_r} \frac{\tau_r}{\tau_f} (\tau - \tau_r - \tau_f)^{3/2} \right\} \quad (\text{A-25})$$

Here,  $u(\tau)$  is the unit step function (Heaviside function) that vanishes when its argument is negative and is unity when its argument is positive. The purpose of these step functions is to ensure that none of each of the three terms contributes anything unless its own  $\tau_j$  is positive.

Recall that the time-like variables in (A-25) have been defined as  $\tau = D_{\text{th}} t$ , where  $t$  is the actual time variable, and  $D_{\text{th}} \equiv \kappa/\rho C$ . At this point, it is convenient to redefine the time-like variables so as to be normalized to the rise-time  $t_r$ . Thus, we shall define a new  $\tau$ , and a new  $\tau_f$  by

$$\tau \equiv t/t_r ; \quad \tau_f \equiv t_f/t_r . \quad (\text{A-26})$$

In terms of these new time-like quantities, Eq. (A-25) may be re-expressed as follows.

$$T(0, \tau) = \frac{q_{\max}}{\Gamma(\frac{5}{2})} \sqrt{\frac{t_r}{\kappa\rho C}} \left\{ u(\tau) \tau^{3/2} - u(\tau - 1) (1 + \tau_f^{-1}) (\tau - 1)^{3/2} + u(\tau - 1 - \tau_f) \tau_f^{-1} (\tau - 1 - \tau_f)^{3/2} \right\} \quad (\text{A-27})$$

Finally, when one notes that  $\Gamma(\frac{5}{2}) = \frac{3}{4}\sqrt{\pi}$ , Eq. (A-27) becomes the same as the expression for the surface temperature excursion that is given in the main body of this report as Eq. (4.1), together with Eqs.(4.2) and (4.3).

The maximum temperature excursion thus occurs at the time when the factor,  $\{...\}$  in Eq. (A-27), is maximized. Denoting  $\{...\}$  by  $f(\tau, \tau_f)$ , it is easy to see that  $f(\tau, \tau_f)$  has a single maximum, which occurs when  $1 < \tau < 1 + \tau_f$ . The specific time of occurrence of this maximum can be found as  $\tau \equiv \tau_{\text{peak}} = (1 + \tau_f)^2 / [(1 + \tau_f)^2 - \tau_f^2]$ , which is plotted in Fig. 9 as a function of  $\tau_f$ . The value of  $f(\tau_{\text{peak}}, \tau_f)$ , that is, the maximum value, is plotted in Fig. 8 as a function of  $\tau_f$ .

## Appendix B

### Plasma Heating

#### B-1: INTRODUCTION

In this Appendix we shall sketch several processes that may contribute to plasma heating in the CTX device. A recurrent theme shall be that the ions receive the primary heating in the very process of ion production and entrainment, which they then share with the electrons by classical equipartition. However, it is recognized that certain supplementary processes involving microinstabilities may also play significant roles in electron heating, and these will be discussed in a later write-up. The consequences of these hypothetical descriptions prove to be consistent with experimentally inferred energy fluxes to the anode, with measured electron temperatures, and with measured neutral particle transverse energies in the plume.

#### B-2: ION ENTRAINMENT HEATING

Let us now consider the process of ion heating associated with ion creation and entrainment. To set the stage, we shall focus on some simple examples.

First, consider two identical blocks, an “active” block  $A$  of mass  $M$  and a “passive” block  $B$  of mass  $M$ , each free to move on a common linear track without friction. The active block  $A$  contains a perfect motor that guarantees the constant velocity of block  $A$  in all circumstances, say  $v_A$  in the laboratory frame. (Alternatively, one could imagine that only  $A$  is rigidly attached to a constant-velocity conveyor belt.) Suppose block  $B$  is initially at rest (in the laboratory frame) in the path of oncoming block  $A$ . As viewed from  $A$ ,  $B$  is approaching with velocity magnitude  $v_A$ . Let us now consider two kinds of collision of these two blocks, a perfectly elastic collision and a perfectly inelastic collision.

In a perfectly elastic collision, all of the elastic potential energy stored in the compressed material during the collision of  $A$  and  $B$  is returned to the kinetic energy of the center of mass of  $B$ , which then recedes from the (motionless) block  $A$  with velocity  $v_A$ . In the lab frame,  $A$  continues with the constant velocity  $v_A$ , whereas  $B$  now moves ahead of  $A$  with velocity  $2v_A$ . In the lab frame the



total momentum of the two-block system has tripled, and the total energy of the system has quintupled (thanks to the work done by the motor during the collision).

However, in a perfectly inelastic collision, block B acts like a blob of putty, which sticks to A after the collision. Considered in the frame of A, all of the elastic potential energy that should have been built up during the collision,  $\frac{1}{2} M v_A^2$ , becomes distributed instead into many internal degrees of freedom, i.e., heat energy, and therefore none is available to be returned to the center-of-mass motion of B relative to A. In the lab frame, the momentum of the system has doubled, the kinetic energy of gross motion has doubled, and an amount of heat energy has been created that equals the additional kinetic energy.

This simple example of a two-body collision illustrates the point that when matter at rest is entrained into a constant-velocity system, it must be heated by an amount equal to the additional kinetic energy that is created.

Another example of this process is well known from ordinary gas dynamics. In the process of a strong planar shock impinging upon a compressible gas which is at rest in the lab frame, the conservation laws of mass, momentum, and energy across the shock can be utilized to show that the thermal energy density behind the shock,  $P/(\gamma - 1)$ , equals the kinetic energy density behind the shock,  $\rho V^2/2$ . Here,  $P$  and  $\rho$  are respectively the post-shock gas pressure and mass density, and  $V$  is the post-shock gas velocity in the lab frame. (This result can be obtained, for example, from the high-Mach-number limit of the expressions displayed in *Fluid Mechanics* (2nd edition), by L. D. Landau and E. M. Lifshitz, Pergamon Press (1987), Chap. IX—Shock Waves.)

The presence of a sharp interface is not essential for this equipartition of flow energy and thermal energy. For, consider a uniform gas which is being legislated (by a distributed motor) to maintain a constant and uniform velocity  $V$ , and to which mass is being added uniformly at a rate  $\dot{\rho}$  per unit volume. The rate (per unit volume) at which momentum is being created is

$$\dot{\rho} V = f \quad , \quad (\text{B-1})$$

wherein “ $f$ ” is the externally legislated force-density analogous to the “motor” of the two-block collision example. The rate (per unit volume) at which flow kinetic energy is being created is

$$\frac{1}{2}\dot{\rho}V^2 \equiv \dot{W}_K . \quad (\text{B-2})$$

But the rate (per unit volume) at which the motor is performing work is

$$fV = \dot{\rho}V^2 \equiv \dot{W}_M = 2\dot{W}_K . \quad (\text{B-3})$$

Thus, only half of the work done by the motor becomes converted into flow energy. The other half of the work done must therefore be converted into heat energy, since this is the only other energy channel that exists.

Let us finally consider the process of ion heating from the viewpoint developed above, especially within the context of the Los Alamos CTX device. This device, like all MPD thrusters, with or without applied magnetic fields, is basically a crossed-field plasma accelerator. The voltage applied across the coaxial electrodes, in combination with the extant self and applied magnetic fields, forces the ion guiding centers to move with the local  $(\vec{E} \times \vec{B}/B^2)$  drift velocity. (Here,  $\vec{E}$  and  $\vec{B}$  are respectively the local electric and magnetic field vectors.) In the case of self-field thrusters, the  $(E_r/B_\theta)$  guiding center drift is downstream; whereas, for thrusters with strong applied magnetic fields, it is primarily azimuthal  $(E_r/B_z)$  pending its conversion to downstream motion by a diverging nozzle. But, in either case, the actual ion trajectories themselves are well known to be basically cycloidal, that is, having a circular gyration at the ion gyro-frequency superposed about the motion of the guiding center. (The ion gyro-frequency is  $(eB/m_i)$  in MKS units, for an ion of charge  $e$  and mass  $m_i$ .)

Let us now consider the special character of such cycloidal orbits belonging to ions that have been created from resting neutrals (or from neutrals with velocities small compared to  $(E/B)$ ). Such ions find themselves to be suddenly entrained in a moving electrodynamical system characterized by the  $(E/B)$  velocity. The only cycloidal orbits that satisfy the initial condition that the ions must start from rest are those that resemble a point on the rim of a coin standing on edge rolling on a table. Such orbits have the trivially obvious but very important property that their gyro-velocities are equal in magnitude to their common guiding center drift velocities. For a local ensemble of ions created at random from resting neutrals, these gyro-orbits have random phases and therefore can be regarded as comprised of random thermal velocities superposed on the flow velocity. In

the absence of frequent collisions, one has two degrees of freedom, hence  $\gamma = 2$ . The thermal energy density of the ions is thus

$$(\gamma - 1)^{-1} P_i = n_i T_i = \frac{m_i}{2} n_i \left( \frac{2T_i}{m_i} \right) = \frac{m_i}{2} n_i v_{thi}^2, \quad (\text{B-4})$$

which is the same as the flow kinetic energy density for these orbits since  $v_{thi} = E/B$ . (Here  $P_i$  is ion pressure perpendicular to  $\vec{B}$ ,  $n$  is ion number density,  $T_i$  is ion temperature, and  $v_{thi}$  is ion “thermal velocity.”) Although one has a cylindrical-shell distribution function rather than a Maxwellian, the “thermal” pressure effects across  $\vec{B}$  are close enough that the analogy is useful, and Eq. (B-4) can be regarded as defining the ion temperature for these orbits wherein  $v_{thi} = E/B$ . In fact, the exact Eq. (B-4) can be directly derived for the ion pressure associated with a cylindrical shell distribution function  $f_i(\vec{u}) = (n_i/\pi)\delta(u_\perp^2 - v_{thi}^2)\delta(u_z)$ , where the velocity vector  $\vec{u}$  represents the difference between the particular velocity and the average velocity, with the local  $z$ -direction along  $\vec{B}$ . Thus, in this generalized sense, the thermal energy density of ions, created from resting neutrals in a crossed-field plasma accelerator, equals their flow energy density. (Note that it was not necessary to invoke collisionality here, which serves to emphasize just how fundamental is this equipartition between flow energy and thermal energy during entrainment heating.)

All of the above examples illustrate the fundamental process of entrainment heating, but to complete this discussion of ion heating in the CTX device we must now deal with those thus-far-suppressed topics of electron-ion interactions, ion viscous heating, and ion thermal conduction losses. These processes, in conjunction with the inelastic process of ion entrainment, all contribute to setting the level of the ion temperature. These topics will now be dealt with in connection with 40 MW class operation of the CTX device.

By taking moments of the Boltzmann equation for the ion phase-space distribution function, while allowing for the creation of ions from *resting* neutrals, one can obtain the following equation governing the evolution of ion temperature,  $T_i$ .

$$\frac{1}{\gamma - 1} \frac{dT_i}{dt} + T_i \nabla \cdot \vec{V}_i = \left( \frac{\dot{n}}{n} \right) \left( \frac{1}{2} m_i V_i^2 - \frac{1}{\gamma - 1} T_i \right) + \dots \quad (\text{B-5})$$

Here,  $\vec{V}_i$  is the ion flow velocity,  $(\dot{n}/n)$  is the local ion production rate per ion (usually dependent on the electron temperature,  $T_e$ ),  $\frac{d}{dt}$  is the total convective

derivative,  $\left(\frac{\partial}{\partial t} + \vec{V}_i \cdot \nabla\right)$ , and the dots ( $\dots$ ) signify the additional complicating effects of electron-ion equipartition of thermal energy, ion viscous heating, and ion thermal conduction losses. We shall presently discuss each of these topics as it influences the ion temperature. (The thermal source term,  $m_i V_i^2/2$ , eventually disappears downstream by the time neutrals may have been accelerated up to the ion flow velocity.)

But first, it is of interest to remark that if none of these complicating effects are dominant, then the mathematical structure of Eq. (B-5) already provides to us information that supplements the simple guiding center model described earlier. Namely, if  $\nabla \cdot \vec{V}_i$  also does not dominate, then Eq. (B-5) indicates the tendency for the ion temperature to “settle in” at the level of the ion flow energy (per particle), in accordance with the simple model of entrainment heating; and moreover that the relaxation time for a deviated  $T_i$  to approach this special value is determined by the ion production rate (per ion). (See also H. A. Hassan, *Physics of Fluids* **9** (1966) 2077.) Thus, Eq. (B-5) essentially verifies the inelastic heating and the equipartition of ion flow energy and ion thermal energy due to the ion production and entrainment process, and it yields a characteristic time scale for such heating; but it also confronts us with modifications and qualifications to the simple picture that have to be considered.

With regard to electron-ion temperature equipartition in the CTX device, it can be observed here that, if the ion temperature is indeed near the flow energy, then calculations to be presented in a subsequent write-up show that equipartition with electrons is, in fact, a modest effect, thus being *a posteriori* consistent with the provisional neglect of this effect in Eq. (B-5). But even in the presence of rapid temperature equipartition between ions and electrons, conclusions can be drawn similar to those already presented here. An equation assuming rapid electron-ion equipartition (but neglecting the Hall effect and assuming that the plasma is optically thick to excited-state decay radiation) has been derived elsewhere that is a generalization of Eq. (B-5) to include excitation and ionization processes in hydrogen. (See “Preliminary Scoping Studies for Nozzle-based Coaxial Plasma Thrusters,” by R. A. Gerwin, K. F. Schoenberg, and D. J. Rej; in Eighth Symposium on Space Nuclear Power Systems, Albuquerque, 1991; Proceedings Pub. by American Institute of Physics, AIP Conf. Proc. 910116; Part Two, p. 493.) This equation can be expressed schematically

as

$$\frac{2}{\gamma - 1} \frac{dT}{dt} + 2T \nabla \cdot \vec{V}_i = (\text{effective rate}) \left( \frac{1}{2} m_i V_i^2 - \frac{2}{\gamma - 1} T - \Delta E \right) + \dots, \quad (\text{B-6})$$

wherein  $T$  is the common electron-ion temperature and  $(\dots)$  again refers to viscous and resistive heating and thermal conduction loss terms. (Near to a steady state, it can be demonstrated that the effective production rate is practically the rate of electron impact generation of excited hydrogen states.) The important new element in Eq. (B-6) is the appearance of  $\Delta E$ , an energy increment characteristic of electron-impact-induced atomic transitions that also generally depends on the relative population levels and  $T$ -dependent rate coefficients. In hydrogen near to a steady state, it can be shown that  $\Delta E$  will be of order 10 eV. The mathematical structure of Eq. (B-6) contains the features of a “critical ionization velocity” process, in the sense that if the flow energy is too small,  $T$  will fall and not produce more ionization; whereas if the flow energy is sufficiently large, then  $T$  can rise to a level that continually produces ionization. (See H. Alfvén, “Collision Between a Non-ionized Gas and a Magnetized Plasma,” *Rev. Mod. Phys.* **32** (1960) 710.) In fact, if the flow energy is sufficiently large against  $\Delta E$ , then Eq. (B-6) implies, as before, that “the thermal energy will saturate near the flow energy.” In the present case of rapid equipartition, however, it is the thermal energy of an electron-ion pair that would saturate near the flow energy of an ion.

In the CTX device at 40 MW operation, guiding-center drift energies in the breech are inferred to be about 25 eV, and axial neutral energies in the plume have been measured at upwards of 100 eV. In view of the above discussion, it may therefore not be unrealistic to expect “ion entrainment heating” at a thermal level of at least 25 eV in these experiments. However, the production and sustainment of such an ion temperature is subject to consideration of ion viscous heating and thermal conduction losses, upon which we now embark.

### B-3: ION VISCOUS HEATING AND THERMAL CONDUCTION COOLING

Within the context of 40–50 MW operation of the CTX device, measured densities at the muzzle ( $\sim 1.0 \times 10^{20} \text{ m}^{-3}$ ), self-magnetic field strengths (6 –

$8 \times 10^{-2}$  tesla), and 25 eV or higher ion temperatures according to the ion entrainment model, when taken all together imply that the deuterium ions are well-magnetized.

$$\omega_{ci}\tau_{ii} \sim 10 .$$

(Here,  $\omega_{ci}$  is the ion gyro-frequency and  $\tau_{ii}$  is the ion-ion collision time. The ion-ion collision frequency is written as  $\nu_{ii} = \tau_{ii}^{-1}$ .) Moreover, since the axial transit time is only a few  $\mu\text{s}$  (based upon the measured axial velocity of neutrals of about  $10^5$  m/s and upon the indication of electrode wear along a 10–30 cm axial distance), there can be only a few ion-ion collisions during an axial transit time  $t_z$ .

$$t_z\nu_{ii} \sim \text{a few}.$$

Therefore, a strongly-magnetized, almost collisionless model for the ion behavior is appropriate, provided also that ion-neutral collisions are negligible. (There is, at present, no information regarding the density of neutrals during the CTX discharge.) Such a model for the ions shall be used here to estimate the effects of ion viscosity and ion thermal conduction. A very detailed and complete reference on this subject, transport coefficients of fully ionized plasmas, exists. (S. I. Braginskii, "Transport Processes in a Plasma," in *Reviews of Plasma Physics*, Vol. 1, Consultants Bureau, M. A. Leontovich, Ed., New York (1965).) We shall use the results of Braginskii for strongly magnetized ions.

Suppose there exists a radial gradient (width  $\delta_r$ ) of axial velocity ( $V_z$ ), due to a no-slip boundary condition. Then, one can estimate that the *fractional* increase of ion temperature due to viscous heating during an axial transit (length  $\Delta_z$ ) is given by

$$0.3 \frac{1}{(\omega_{ci}\tau_{ii})^2} \left( \frac{V_z\tau_{ii}}{\delta_r} \right) \left( \frac{\Delta_z}{\delta_r} \right) \quad (\text{viscous ion heating}). \quad (\text{B-7})$$

For  $(\omega_{ci}\tau_{ii})^2 \sim 100$ ,  $V_z \sim 10^7$  cm/s,  $\Delta_z \sim 10$  cm (nominal),  $\delta_r \sim 2$  cm ( $\delta_r \sim$  half of the channel half-width and also two gyro-radii),  $\tau_{ii} \sim 2 \times 10^{-6}$  s, the above expression becomes

$$(\text{viscous ion heating}) \sim 0.15 . \quad (\text{B-7-a})$$

Suppose there exists a radial gradient (width  $\delta_r$ ) of ion temperature  $T_i$ . Then, one can estimate that the *fractional* loss of ion temperature due to cross-field thermal conduction during an axial transit is given by

$$\frac{\tau_{ii}}{(\omega_{ci}\tau_{ii})^2} \frac{(2T_i/m_i)}{\delta_r^2} \frac{\Delta_z}{V_z} = \frac{1}{(\omega_{ci}\tau_{ii})^2} \left( \frac{v_{thi}\tau_{ii}}{\delta_r} \right) \left( \frac{v_{thi}}{V_z} \right) \left( \frac{\Delta_z}{\delta_r} \right) \quad (\text{thermal conduction ion cooling}). \quad (\text{B-8})$$

Using the same parameters as above, and with  $v_{thi} = 0.5 \times 10^7$  cm/s corresponding to  $E/B$  in the breech, this expression reduces to

$$(\text{thermal conduction ion cooling}) \sim 0.13 \quad . \quad (\text{B-8-a})$$

The first thing to notice about these estimates is that they are each small fractions of the estimated ion temperature; secondly, they are almost equal in magnitude; and thirdly, these two processes tend to cancel one another. We therefore conclude that the simultaneous omission of these two processes in the consideration of Eq. (B-5) is justified.

Now, these two numerical estimates depended upon assumptions in CTX regarding gradient scale lengths, and axial transit distances; and they would become individually larger in regions of sharper gradients (smaller  $\delta_r$ 's) or larger axial transits (larger  $\Delta_z$ 's). However, both expressions scale identically, as  $\Delta_z \delta_r^{-2}$ , so that their mutual cancellation would be retained. Moreover,  $\delta_r$  itself cannot be much smaller than already assumed, since the ion gyro-radius under the given conditions is about 1 cm.

Note that the ratio of viscous heating (B-7) to conduction cooling (B-8) is about  $V_z^2/(3v_{thi}^2)$ . Since  $V_z$  represents a flow velocity in the nozzle ( $\sim V_A$ ) which has begun to be accelerated beyond the drift velocity in the breech, one might expect that this ratio is always of order unity—as can be experimentally inferred. (We are tacitly assuming here that  $v_{thi}$  represents the ion temperature of particles entrained upstream that have been swept into the nozzle region from the breech. This assumption is *a posteriori* consistent with the estimate that net heating or cooling effects on the ions during their journey from breech to nozzle are small-to-moderate.)

## Appendix C

### Inframetrics IR Camera Calibration

The Inframetrics model 600 IR video camera measures temperature change on a target surface by measuring changes in infrared emission from that surface over a 9 to 11 micron bandwidth. The infrared intensity reaching the camera is the sum of radiation emitted by the target and the background radiation reflected off the target. Here, the radiation emitted by the target is the Planck black-body function integrated over the bandwidth and weighted by the target emissivity  $\epsilon$ . The reflected radiation is related to the background temperature weighted by the target reflectivity  $(1-\epsilon)$ .

In many applications, the background temperature is uniform and static in time. Hence, an absolute conversion of the emitted IR radiation into temperature simply requires a value for the target emissivity and the background temperature. During CTX discharges, however, all electrode surfaces are heated by the plasma. Hence, the nominal background temperature is both time dependent and near that of the imaged electrode surface. For this case, the camera “emissivity parameter” and “background temperature parameter” are ill-defined.

Absolute calibration of the IR camera, for CTX relevant conditions, entailed uniformly heating the thruster to 65° C using hot air. The camera was then positioned to replicate the spatial line-scans used to acquire the reported data. As the electrodes slowly cooled, covering the range of data-relevant temperature changes, true electrode temperature was monitored by a thermocouple attached to the anode (at the position of the line-scan). The camera “emissivity parameter” was then continuously adjusted to force agreement between the camera inferred temperature and that of the thermocouple. Here, the camera “background temperature parameter” was set at 20° C. In this way, a calibration “curve” was generated that permitted conversion of imaged IR intensity into electrode temperature. This calibration procedure did not account for the effects of differences in electrode temperature or spatially distributed electrode temperature. Both these effects are considered small for the CTX data reported.



---

Table I. Parameters and Peak Energy Flux Estimates for 40-MW-Class Shots

---

Shot #	$t_r(\mu s)$	Peak Power (MW)	$t_f(\mu s)$ (10% of Peak Power)	$\tau_f$	$f_{max}$ ( $1 + .13\tau_f$ )	$(\Delta T)_{max}$ ( $^{\circ}C$ )	$q_{max}$
20274	100	50	330	3.30	1.43	11.7	23
20280	100	60	300	3.00	1.39	7.2	14
20291	100	40	420	4.20	1.55	13.5	24
20300	90	45	400	4.44	1.58	11.7	22
20301	100	50	340	3.40	1.44	15.3	30
20338	100	40	450	4.50	1.59	12.6	22
20340	75	48	420	5.60	1.73	12.6	23
20341	110	50	360	3.27	1.43	8.1	15
20342	110	50	360	3.27	1.43	9.9	19
20373	100	43	425	4.25	1.55	13.5	24
20375	100	46	400	4.00	1.52	15.3	28
20377	85	50	440	5.17	1.67	18.9	34

---

Assuming  $(\Delta T)$  ( $^{\circ}C$ ) at  $t = 0.5$  ms is  $(\Delta T)_{max}$  ( $^{\circ}C$ ).

mean power:  $\bar{p} = 48 \pm 5$  MW

mean:  $\bar{q}_{max} = 23 \pm 5$  [MW/m<sup>2</sup>]

---

---

Table IA. Peak Energy Flux Estimates for 40-MW-Class Shots

---

Shot #	$\tau(500\mu s)$	Peak Power (MW)	$\tau_f$	$f(\tau, \tau_f)$	$q_{max}(\text{MW}/\text{m}^2)$
20274	5.0	50	3.30	0.93	35
20280	5.0	60	3.00	0.85	24
20291	5.0	40	4.20	1.28	30
20300	5.6	45	4.44	1.18	29
20301	5.0	50	3.40	0.96	45
20338	5.0	40	4.50	1.40	25
20340	6.7	48	5.60	1.31	31
20341	4.5	50	3.27	1.03	21
20342	4.5	50	3.27	1.03	26
20373	5.0	43	4.25	1.30	29
20375	5.0	46	4.00	1.18	36
20377	5.9	50	5.17	1.39	41

---

Assuming  $(\Delta T)$  ( $^{\circ}\text{C}$ ) at  $t = 0.5$  ms is not  $(\Delta T)_{max}$  ( $^{\circ}\text{C}$ ).

$$q_{max} \left[ \frac{\text{MW}}{\text{m}^2} \right] = \frac{2.8}{\sqrt{t_r[100\mu s]}} \frac{\Delta T[^{\circ}\text{C}]}{f(\tau, \tau_f)} ,$$

with  $\tau = \frac{500\mu s}{t_r}$  and  $\Delta T$  ( $^{\circ}\text{C}$ ) measured at  $500 \mu s$ .

mean power:  $\bar{p} = 48 \pm 5$  MW

mean:  $\bar{q}_{max} = 31 \pm 7$  [MW/m<sup>2</sup>]

---

---

Table II. Parameters and Peak Energy Flux Estimates for 10-MW-Class Shots

---

Shot #	$t_r(\mu s)$	Peak Power (MW)	$t_f(\mu s)$	$\tau_f$	$f_{max}$	$(\Delta T)_{max}$	$q_{max}(\text{MW}/\text{m}^2)$
20381	110	12	400	3064	1.47	3.6	6
20382	120	9	320	2.67	1.35	9.0	17
20383	100	15	250	2.50	1.33	7.2	15
20384	100	9	380	3.80	1.49	8.1	15
20385	100	10	350	3.50	1.46	6.3	12
20386	100	10	360	3.60	1.47	6.3	12
20387	100	11	330	3.30	1.43	4.5	9
20388	110	11	350	3.18	1.41	6.3	12

---

Assuming  $(\Delta T)$  ( $^{\circ}\text{C}$ ) at  $t = 0.5$  ms is  $(\Delta T)_{max}$  ( $^{\circ}\text{C}$ ).

mean power:  $\bar{p} = 11 \pm 2$  MW

mean:  $\bar{q}_{max} = 12 \pm 3$  [MW/m<sup>2</sup>]

---

Table IIA. Peak Energy Flux Estimates for 10-MW-Class Shots

$((\Delta T)_{max}$  not assumed to be at 0.5 ms)

Shot #	$\tau(500\mu s)$	Peak Power (MW)	$\tau_f$	$f(\tau, \tau_f)$	$q_{max}(\text{MW}/\text{m}^2)$
20381	4.5	12	3.64	1.20	8.0
20382	4.2	9	2.67	0.88	26
20383	5.0	15	2.50	0.72	28
20384	5.0	9	3.80	1.10	21
20385	5.0	10	3.50	1.00	17
20386	5.0	10	3.60	1.03	17
20387	5.0	11	3.30	0.93	14
20388	4.5	11	3.18	1.00	17

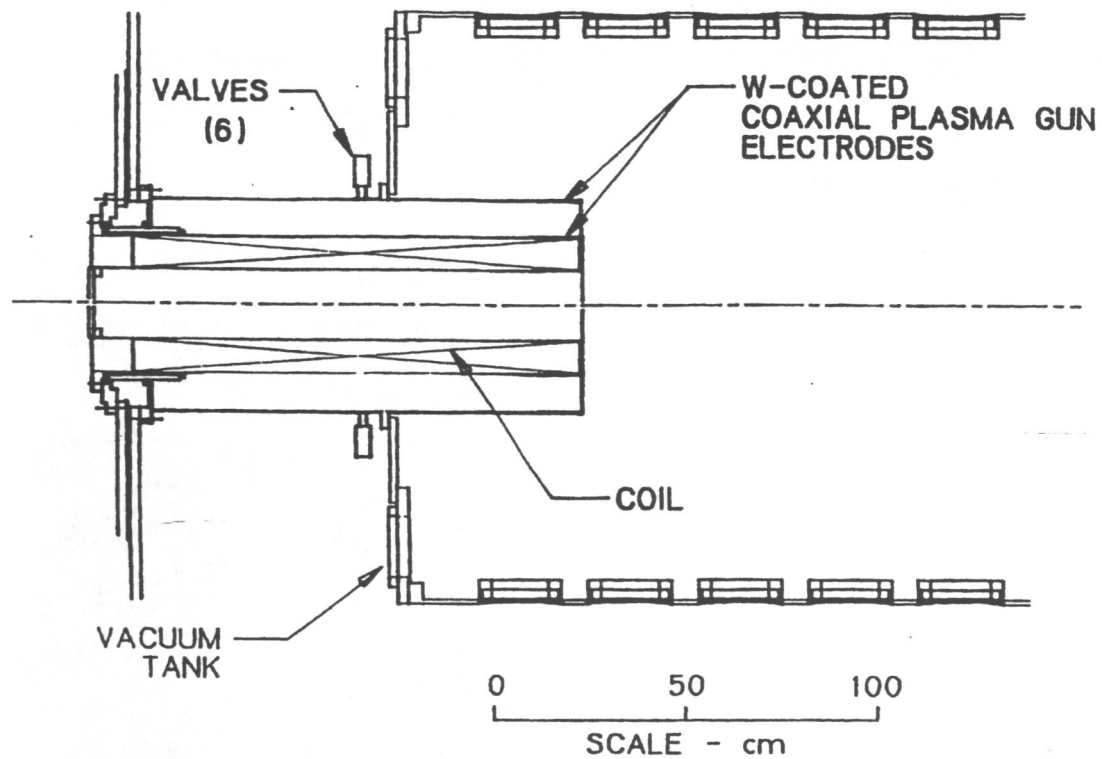
Assuming  $(\Delta T)$  ( $^{\circ}\text{C}$ ) at  $t = 0.5$  ms is not  $(\Delta T)_{max}$  ( $^{\circ}\text{C}$ ).

$$q_{max} \left[ \frac{\text{MW}}{\text{m}^2} \right] = \frac{2.8}{\sqrt{t_r[100\mu s]}} \frac{\Delta T[^{\circ}\text{C}]}{f(\tau, \tau_f)},$$

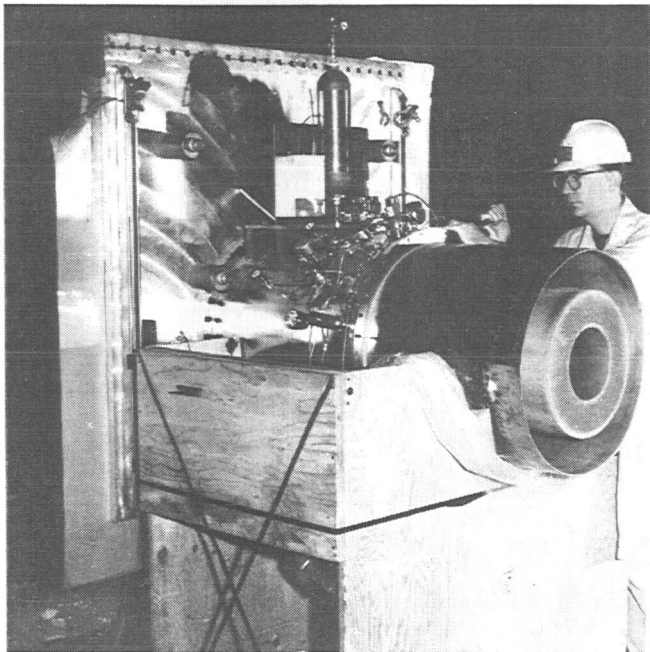
with  $\tau = \frac{500\mu s}{t_r}$  and  $\Delta T$  ( $^{\circ}\text{C}$ ) measured at  $500 \mu s$ .

mean power:  $\bar{p} = 11 \pm 2$  MW

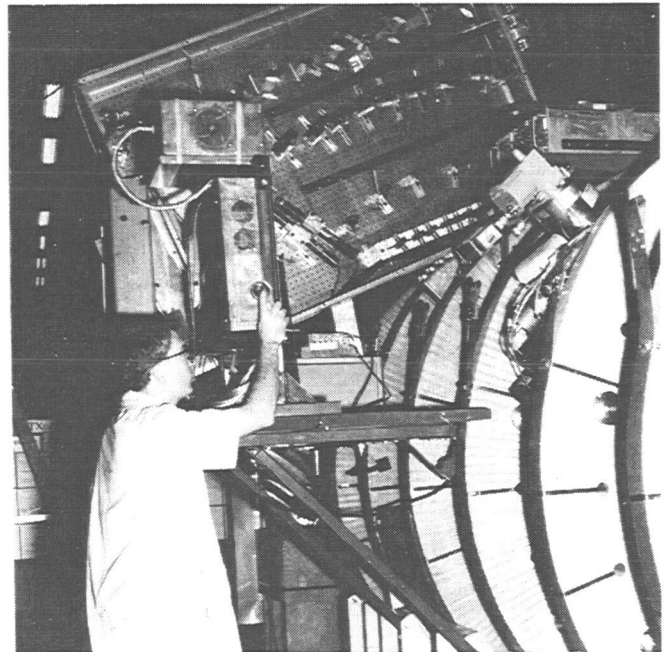
mean:  $\bar{q}_{max} = 18 \pm 5$  [MW/m<sup>2</sup>]



(a) Schematic.



(b) Photograph of the CTX.



(c) Photograph of the CTX facility.

Figure 1.—Coaxial plasma thruster.

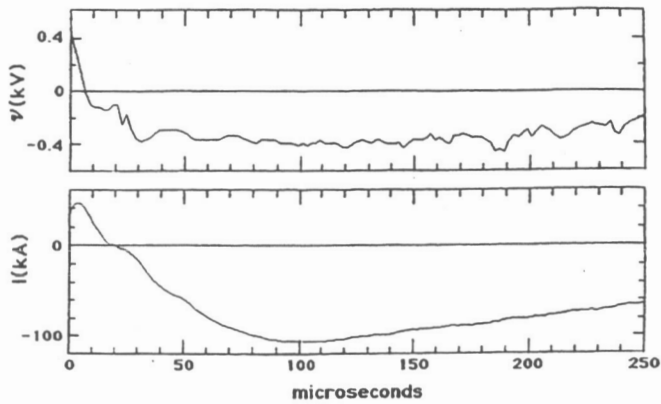


Figure 2.—Nominal "round-top" voltage and current waveforms for a 40 MW discharge.

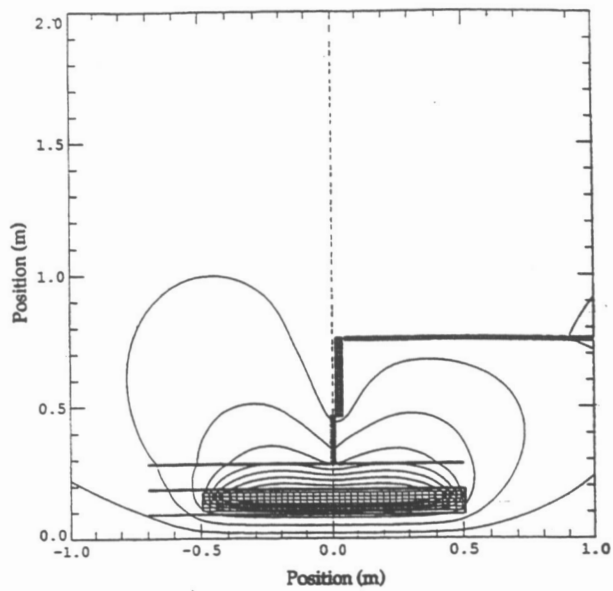


Figure 3.—Vacuum field calculation of applied  $B_{rz}$  magnetic field structure at the time of discharge.

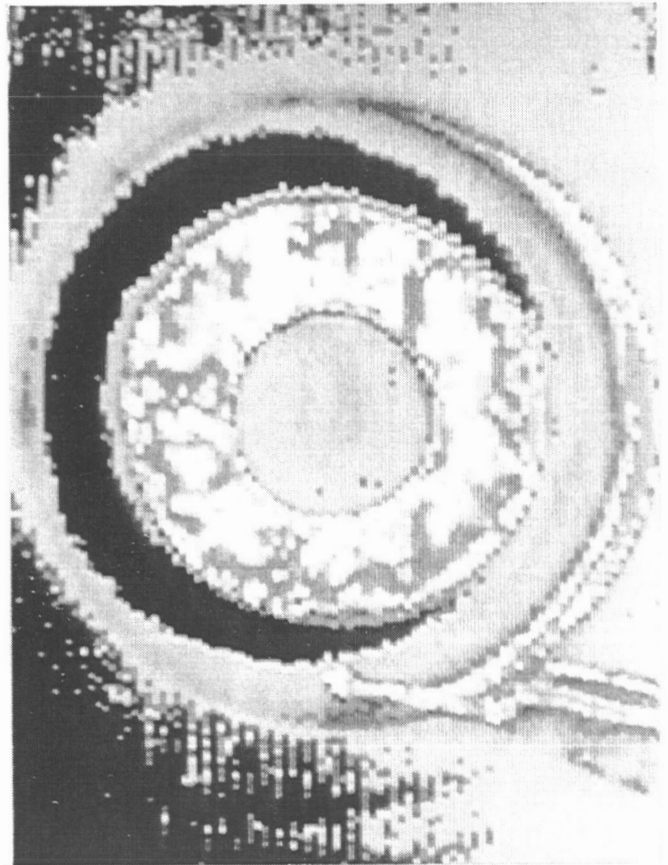
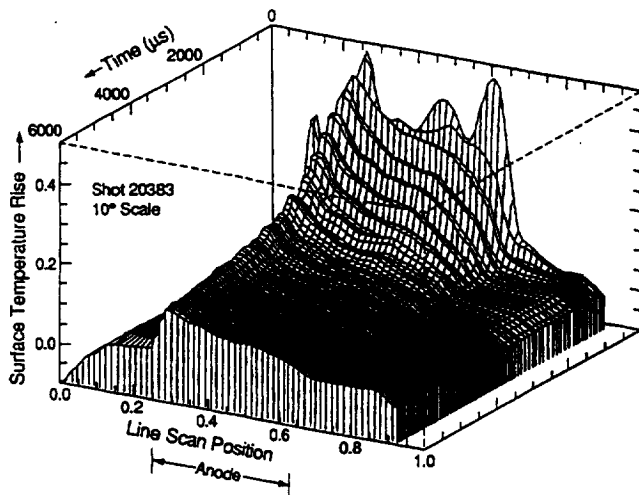
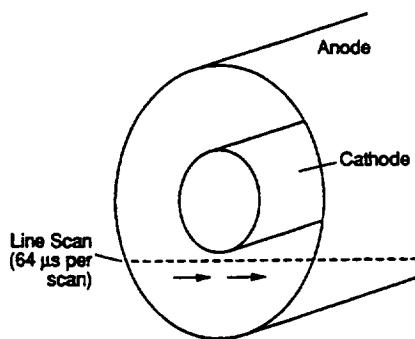


Figure 4.—Infrared image of the CTX coaxial plasma thruster.



(a) Space-time resolved surface temperature rise for discharge 20383.



(b) Position of IR spatial scan line for discharge 20383.

Figure 5.—Discharge 20383.

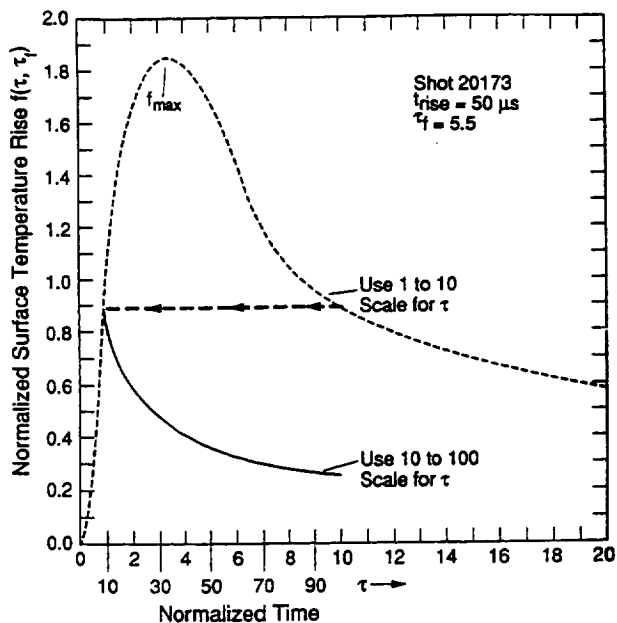


Figure 6.—Time-dependence of normalized surface temperature rise for  $\tau_{fall} = 5.5 \tau_{rise}$ .

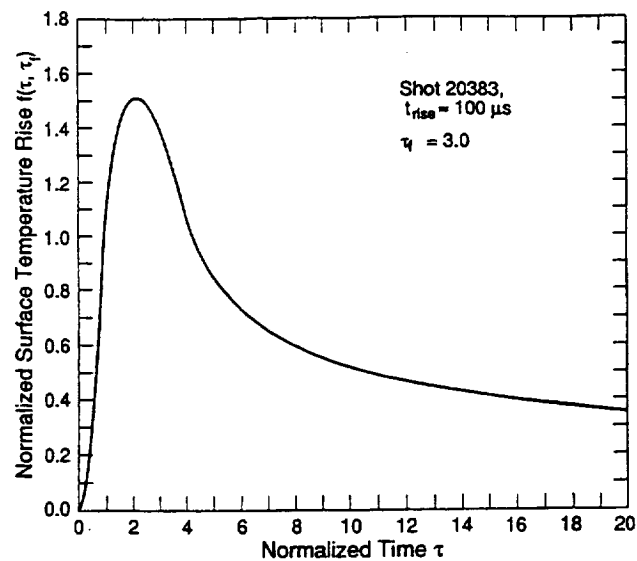


Figure 7.—Time-dependence of normalized surface temperature rise for  $\tau_{fall} = 3.0 \tau_{rise}$ .

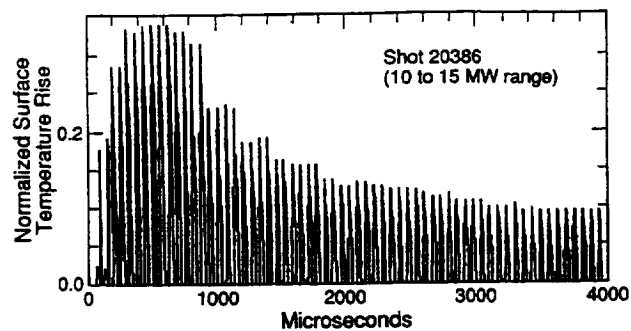


Figure 8.—Data showing surface temperature vs. time. Each narrow vertical strip is a compressed spatial line scan.

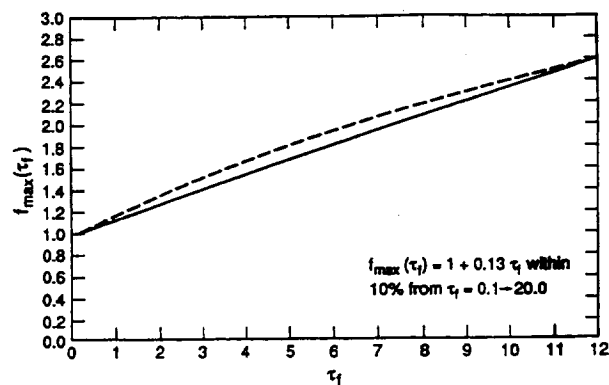


Figure 9.—Normalized peak surface temperature rise vs.  $(\tau_{fall}/\tau_{rise}) = \tau_f$ .

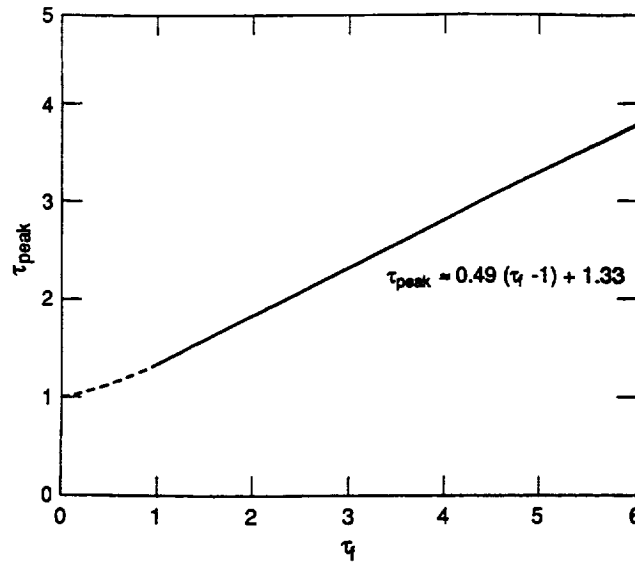


Figure 10.—Normalized time of occurrence of peak surface temperature rise  $\tau_{peak}$  vs.  $\tau_f$  (Eq. (4.6)).

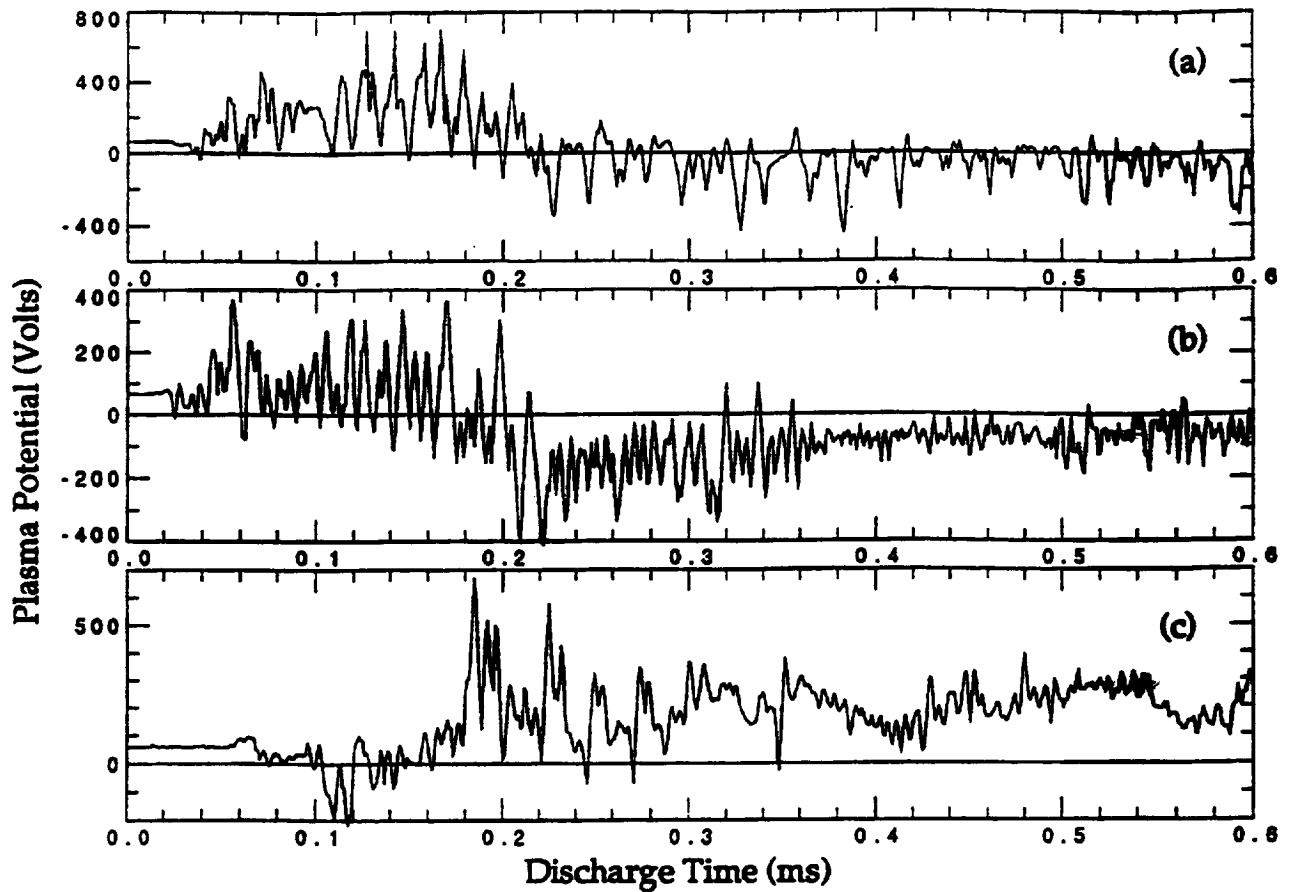


Figure 11.—Plasma potential vs time: (a) probe in muzzle, 1 mm from anode, (b) probe in muzzle, 5 cm from anode, (c) probe 40 cm downstream of thruster exit.



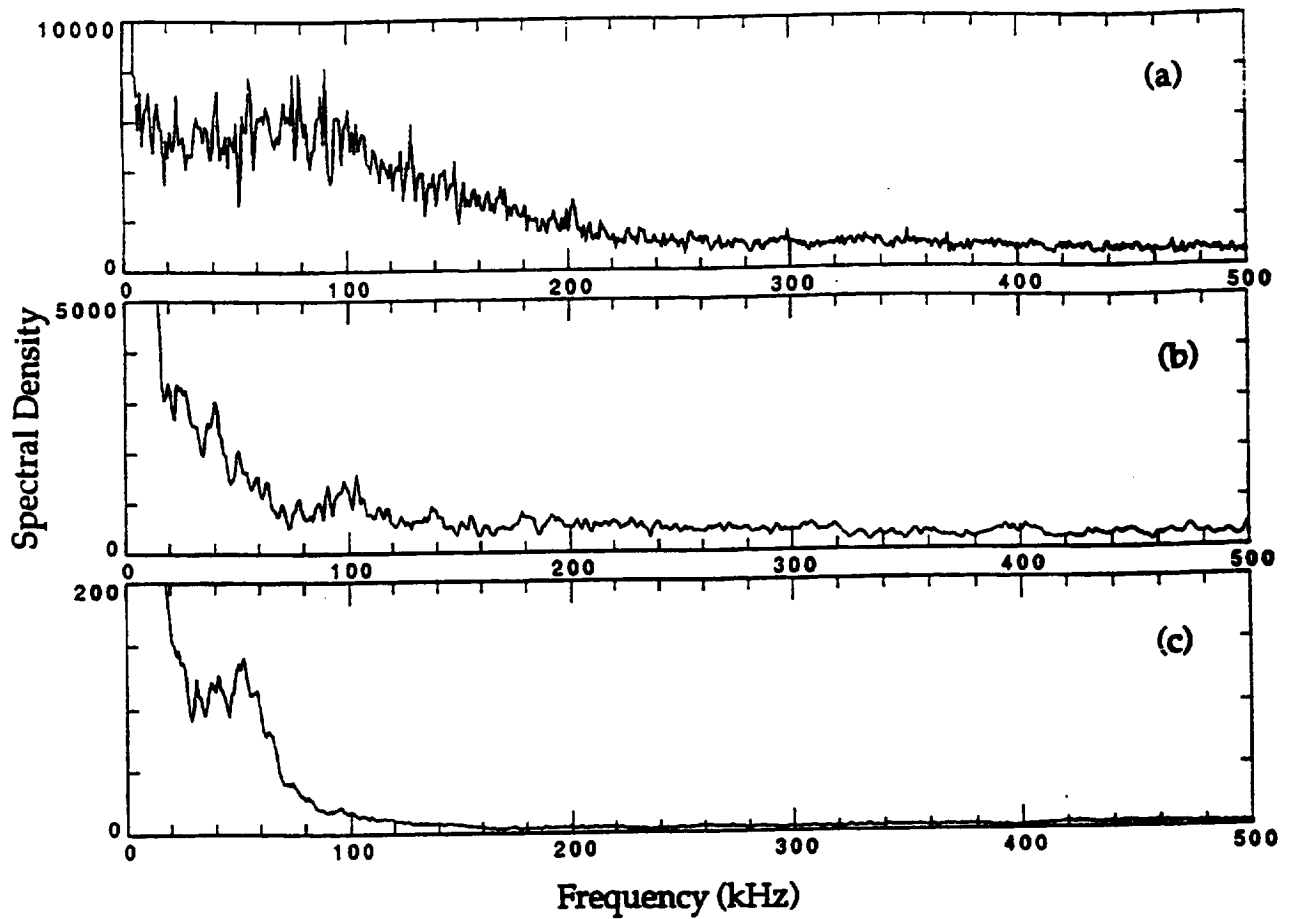


Figure 12.—Power spectral density: (a) plasma potential, (b) applied voltage and (c) interferometer signal (central chord, 40 cm downstream of the exit).

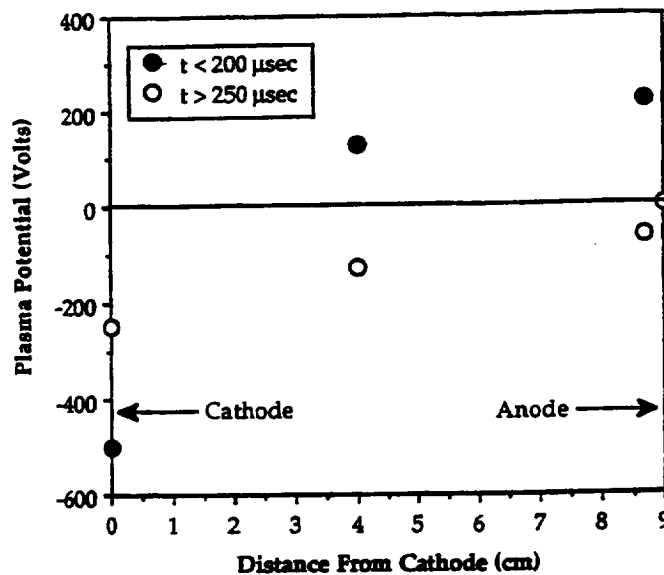


Figure 13.—Radial profile of plasma potential in thruster muzzle for two different periods of the discharge.

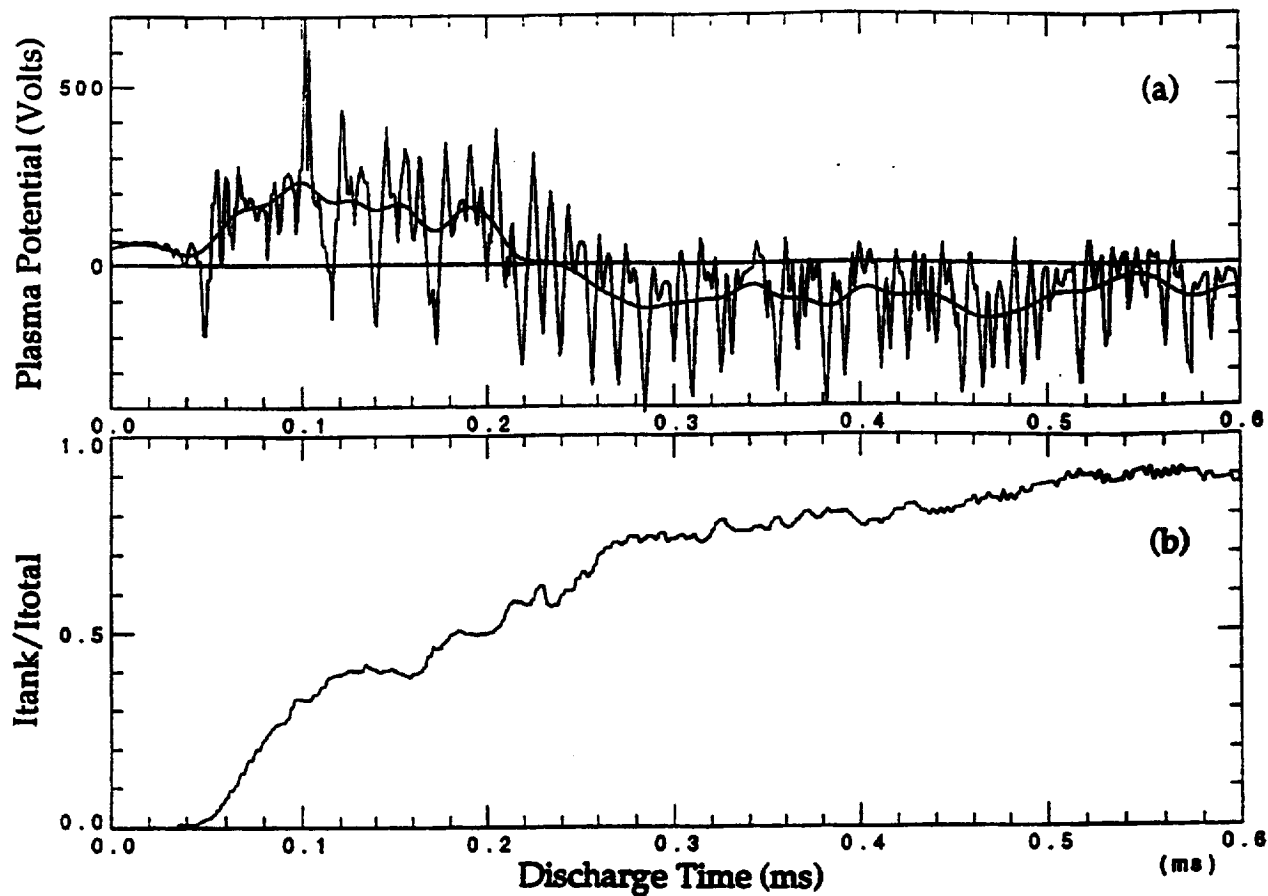


Figure 14.—Plasma potential within the muzzle (also shown is the plasma potential signal following a 20 kHz low pass filter) and fraction of total discharge current flowing through the tank wall.

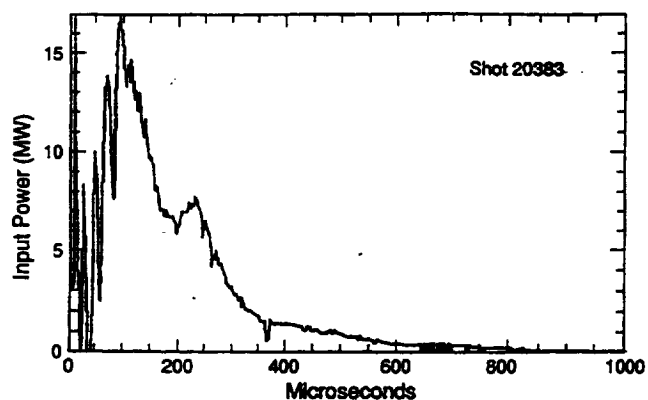


Figure 15.—Input power vs. time for 10 MW discharge 20383.

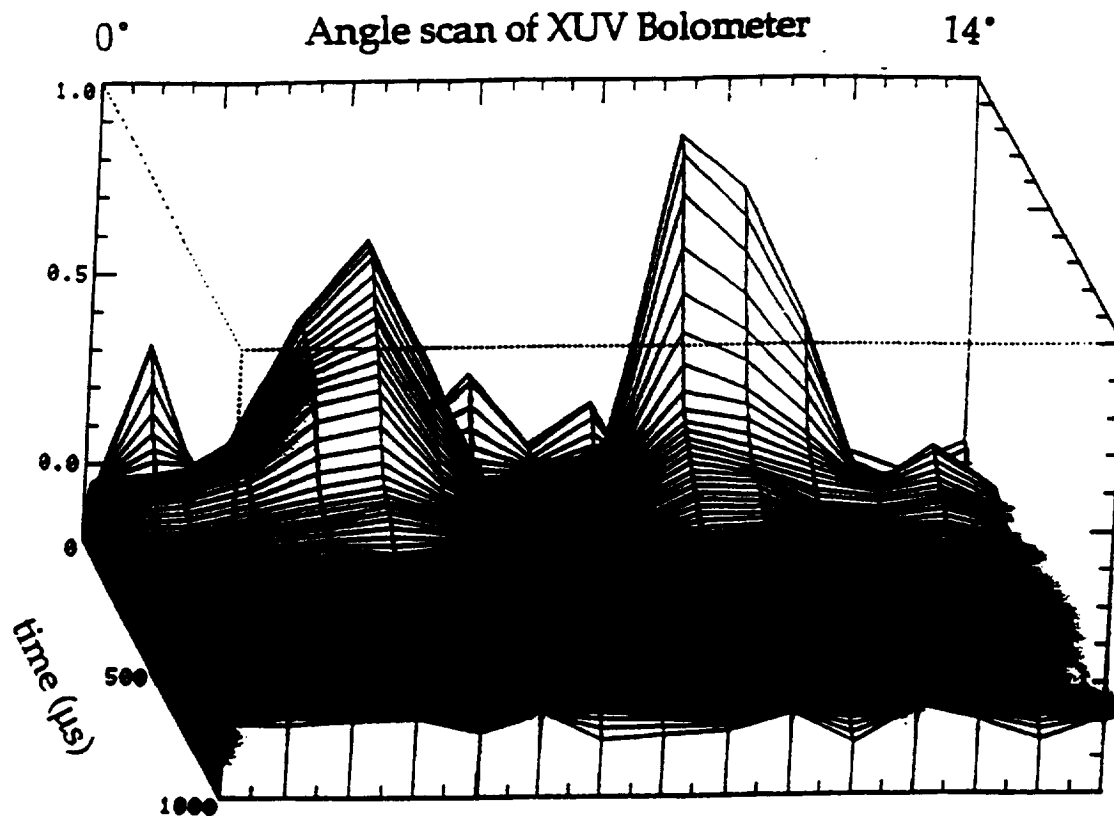


Figure 16.—Radiation profile shows twin peaks across the anode-cathode-anode gaps.

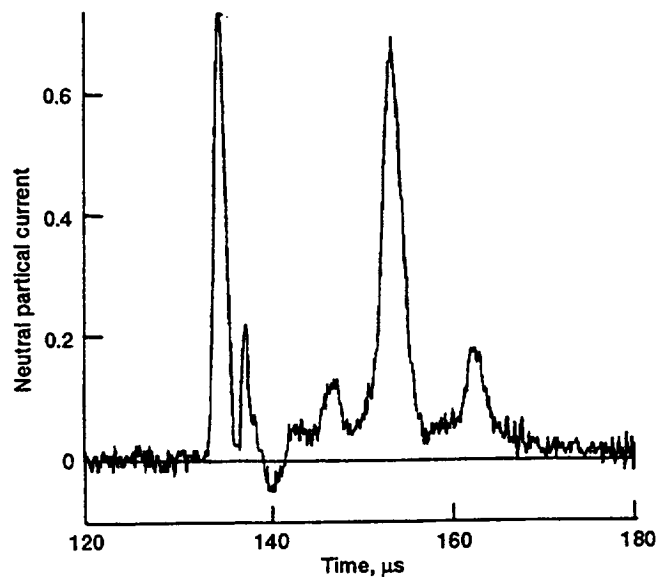


Figure 17.—An arrival time distribution from the TOF neutral particle spectrometer for 40 MW magnetized coaxial gun operation. The temporal difference between the two signal peaks represents the transit time of deuterium neutrals down an approximate 2 meter drift tube.

REPORT DOCUMENTATION PAGE			Form Approved OMB No. 0704-0188	
Public reporting burden for this collection of information is estimated to average 1 hour per response, including the time for reviewing instructions, searching existing data sources, gathering and maintaining the data needed, and completing and reviewing the collection of information. Send comments regarding this burden estimate or any other aspect of this collection of information, including suggestions for reducing this burden, to Washington Headquarters Services, Directorate for Information Operations and Reports, 1215 Jefferson Davis Highway, Suite 1204, Arlington, VA 22202-4302, and to the Office of Management and Budget, Paperwork Reduction Project (0704-0188), Washington, DC 20503.				
1. AGENCY USE ONLY (Leave blank)		2. REPORT DATE March 1993		3. REPORT TYPE AND DATES COVERED Final Contractor Report
4. TITLE AND SUBTITLE Preliminary Investigation of Power Flow and Electrode Phenomena in a Multi-Megawatt Coaxial Plasma Thruster			5. FUNDING NUMBERS  WU-506-42-31 C-NAS3-30065-A	
6. AUTHOR(S)  Kurt Schoenberg, Richard Gerwin, Ivars Henins, Robert Mayo, Jay Scheuer, and Glen Nurdén				
7. PERFORMING ORGANIZATION NAME(S) AND ADDRESS(ES)  Los Alamos National Laboratory Los Alamos, New Mexico 87545			8. PERFORMING ORGANIZATION REPORT NUMBER  E-7628	
9. SPONSORING/MONITORING AGENCY NAMES(S) AND ADDRESS(ES)  National Aeronautics and Space Administration Lewis Research Center Cleveland, Ohio 44135-3191			10. SPONSORING/MONITORING AGENCY REPORT NUMBER  NASA CR-191084	
11. SUPPLEMENTARY NOTES  Project Manager, Roger M. Myers, Space Propulsion Technology Division, (216) 433-7426.				
12a. DISTRIBUTION/AVAILABILITY STATEMENT  Unclassified - Unlimited Subject Categories 20 and 75			12b. DISTRIBUTION CODE	
13. ABSTRACT (Maximum 200 words)  This paper summarizes preliminary experimental and theoretical research that was directed towards the study of quasi-steady-state power flow in a large, un-optimized, multi-megawatt coaxial plasma thruster. The report addresses large coaxial thruster operation and includes evaluation and interpretation of the experimental results with a view to the development of efficient, steady-state megawatt-class magnetoplasma-dynamic (MPD) thrusters.				
14. SUBJECT TERMS  Electric propulsion; Magnetohydrodynamics; Plasma dynamics; Nuclear propulsion			15. NUMBER OF PAGES 58	
			16. PRICE CODE A04	
17. SECURITY CLASSIFICATION OF REPORT Unclassified	18. SECURITY CLASSIFICATION OF THIS PAGE Unclassified	19. SECURITY CLASSIFICATION OF ABSTRACT Unclassified	20. LIMITATION OF ABSTRACT	